Bulletin of the Seismological Society of America, Vol. 100, No. 4, pp. 1427–1455, August 2010, doi: 10.1785/0120090052

Quantitative Comparison of Four Numerical Predictions of 3D Ground Motion in the Grenoble Valley, France

by Emmanuel Chaljub, Peter Moczo, Seiji Tsuno, Pierre-Yves Bard,* Jozef Kristek,
Martin Käser, Marco Stupazzini, and Miriam Kristekova

Abstract This article documents a comparative exercise for numerical simulation of ground motion, addressing the seismic response of the Grenoble site, a typical Alpine valley with complex 3D geometry and large velocity contrasts. Predictions up to 2 Hz were asked for four different structure wave-field configurations (point source and extended source, with and without surface topography). This effort is part of a larger exercise organized for the third international symposium on the effects of surface geology (ESG 2006), the complete results of which are reported elsewhere (Tsuno *et al.*, 2009).

While initial, blind computations significantly differed from one another, a remarkable fit was obtained after correcting for some nonmethodological errors for four 3D methods: the arbitrary high-order derivative discontinuous Galerkin method (ADER-DGM), the velocity-stress finite-difference scheme on an arbitrary discontinuous staggered grid (FDM), and two implementations of the spectral-element method (SEM1 and SEM2). Their basic formulation is briefly recalled, and their implementation for the Grenoble Valley and the corresponding requirements in terms of computer resources are detailed.

Besides a visual inspection of PGV maps, more refined, quantitative comparisons based on time-frequency analysis greatly help in understanding the origin of differences, with a special emphasis on phase misfit. The match is found excellent below 1 Hz, and gradually deteriorates for increasing frequency, reflecting differences in meshing strategy, numerical dispersion, and implementation of damping properties.

While the numerical prediction of ground motion cannot yet be considered a mature, push-button approach, the good agreement reached by four participants indicates that, when used properly, numerical simulation is actually able to handle correctly wave radiation from extended sources in complex 3D media. The main recommendation to obtain reliable numerical predictions of earthquake ground motion is to use at least two different but comparably accurate methods, for instance the present formulations and implementations of the FDM, SEM, and ADER-DGM.

Introduction

The very fact that a large part of the world's populations lives in earthquake-prone areas implies that seismologists must predict earthquake ground motion during potential future earthquakes, no matter whether they can or cannot timely predict earthquake occurrence. Prediction of the earthquake motion at a site of interest is extremely important for designing new buildings and reinforcing existing ones, as well as for undertaking actions that could help mitigate losses during future earthquakes.

Theory and numerical simulation are irreplaceable tools in the earthquake ground-motion research, mainly for two reasons. Considering the present-day limitations of direct controlled physical experiments in seismology, it is extremely difficult to scale laboratory experiments to real structures. Moreover, in most cases, there is a drastic lack of earthquake recordings at the sites of interest.

Given the present state of our knowledge of the processes and structures that form earthquake ground motion, and, at the same time, capabilities of modern seismic arrays, realistic 3D computational models have to include nonplanar interfaces between layers, gradients in velocity, density, and quality

---

*Also at Laboratoire Central des Ponts-et-Chaussées, 58 Bd Lefebvre, 75732, Paris Cedex 15, France.

factors inside layers, and often free-surface topography. In particular, the rheology of the medium has to allow for realistic broadband attenuation. Realistic strong ground-motion simulations should also account for nonlinear behavior in soft soils, which will, however, be neglected here for the sake of simplicity.

Only approximate computational methods are able to account for the structural complexity of the realistic models. The most important aspects of each method are accuracy and computational efficiency (in terms of computer memory and time). These two aspects are in most cases contradictory. A reasonable balance between the accuracy and computational efficiency in case of complex realistic structures made the numerical modeling methods dominant among all approximate methods.

A number of different numerical modeling methods have been developed within the last few decades. Each method has its advantages and disadvantages that often depend on the particular application. Therefore, it is very unlikely that one of the existing or recently developed numerical modeling methods can be systematically and simultaneously the most accurate and the most efficient for all important medium wave-field configurations.

In general, a sufficiently high level of agreement or sufficiently small level of misfit between data and theoretical prediction can be considered a confirmation of a theoretical model of an investigated process. In particular, the agreement between recorded and numerically predicted earthquake motion can be considered an ultimate criterion for capability of seismologists to simulate earthquake ground motion. A procedure of evaluating the capability of the theoretical model to describe the reality can be called validation. Clearly, in the validation it is necessary to understand what is a reasonable level of agreement. Given the complexity and inevitable uncertainty of realistic models (earthquake source and material structure), this is not a simple problem. Certainly, first we have to be sure that the numerical simulation method and its implementation in the computer code are correct. A procedure of evaluating the capability of the method to solve the elastodynamic equations with initial and boundary conditions can be called verification. Without the method verification, it is impossible to properly evaluate the level of agreement between recorded and simulated motions. Consequently, verification of the recent numerical modeling methods for complex realistic models is an important task.

The importance of the objective comparison, verification, and validation of the numerical modeling methods is evidenced by different initiatives. On one hand, the Southern California Earthquake Center (SCEC) has recently organized 3D numerical simulation code validation projects for wave propagation (Day *et al.*, 2003) and dynamic rupture simulations (Harris *et al.*, 2009). The goal was to validate and compare 3D earthquake simulation methods, and foster their application by the engineering community. On the other hand the EU FP6 SPICE project (Seismic Wave Propagation and Imaging in Complex Media: A European Network, www.spice-rtn.org, 2004–2007) aimed at development of computational tools for seismic wave propagation, earthquake motion, and seismic imaging. SPICE has established an open Internet-based digital library (Gallovic *et al.*, 2007; www.spice-rtn.org/library), which comprises computer codes, training materials, simulation exercises, and an interactive web interface for code validation (Moczo *et al.*, 2006; www.nuquake.eu/SPICECVal/). The main goal of the SPICE Code Validation is to provide an open long-term basis for possible tests and comparisons of the numerical methods and codes for the seismic wave propagation and earthquake motion simulations. The objective evaluation of accuracy and comparison is facilitated using the time-frequency misfit criteria (Kristekova *et al.*, 2006) interactively applicable to a solution one wants to compare with any of the previously uploaded solutions.

In parallel, real sites and realistic models were prime targets of the blind prediction tests in framework of three international symposia on the effects of surface geology (ESG) in Odawara, Japan (1992), Yokohama, Japan (1998), and Grenoble, France (2006). The ESG 2006 symposium provided an excellent opportunity to focus on numerical modeling of earthquake motion in the Grenoble Valley for local weak and moderate earthquakes. The Grenoble Valley is a very interesting and typical deep Alpine sediment-filled structure. The Grenoble urban area, mostly built over the sedimentary area, gathers a significant population (around 500,000), a number of high-tech and/or sensitive industrial facilities, and educational and research institutions. Therefore, despite an only moderate regional seismic hazard (with known historical events hardly reaching magnitude 6) and considerable broadband site effects, Lebrun *et al.* (2001) raised the concern about the seismic risk in such Alpine valley configurations, which are also met in different other areas within the European Alps, and in other mountainous areas with embanked valleys filled with young, postglacial lacustrine sediments.

Our article presents results of a multi-institution project and an unprecedented comparison of very different and important methods applied to a structurally complex model of a real site. The scope of our article is not to benchmark computer codes that solve a well-referenced problem with a known analytical solution. Rather, our article considers a realistic 3D problem for which we do not have a reference solution. There is no objective way of defining an absolute level of accuracy for the different predictions of the seismic response of the Grenoble Valley.

The applied methods have been developed by various teams in different institutions using different computer facilities. It was not technically feasible to perform presented simulations on the same computer. It is important to realize that the use of the same computer is of marginal importance compared with the main aspect of the article.

The scope and goal of our article match those of the SCEC code validation project that targeted the Los Angeles basin to demonstrate the reachable level of agreement among the leading U.S. modeling teams. Our article has a similar goal; in addition, it considers a wider set of numerical methods and a significantly higher maximum frequency.

Compared with the Los Angeles basin, the modeling of the Grenoble Valley is complicated by the relatively large velocity contrast and the complex interface geometry. The level of the reached agreement was not possible to anticipate and thus is not trivial.

Structurally complex models of real sedimentary valleys pose great challenges. Even though there have been a number of attempts at validation, the agreement between synthetics and data remains far from satisfactory, except for very low frequencies, say <0.1 Hz. This is because one cannot isolate the validity of the simulation from that of other factors, such as the material model, including possible nonlinearities, and the source description. One common way to reduce the influence of these factors is to use small earthquakes, whose rupture can be modeled as a point source.

Given the model complexity and methodological differences among the applied methods, we found a surprisingly good level of agreement for four of the submitted predictions obtained by different teams: Käser *et al.* (2006) used the arbitrary high-order derivative discontinuous Galerkin method (ADER-DGM), Chaljub (2009) used the spectral-element method (SEM), Kristek *et al.* (2009) used the finite-difference method (FDM), and Stupazzini (2009) and Stupazzini *et al.* (2009) used another implementation of the SEM. The ADER-DGM, FDM, and SEM differ both in the basic formulations of the equations of motion and boundary conditions, and the way they construct discrete models and the resulting systems of algebraic equations. They also differ in the required computer memory and time. At the same time these three methods, together with the finite-element method (FEM), are at present the most powerful numerical modeling methods for earthquake ground motion. Whereas the FDM and FEM have a relatively long tradition, the SEM has been used since the early 1990s; ADER-DGM has been elaborated and applied to seismology rather recently. Despite this relatively long tradition of the FDM and FEM, they are still being developed in terms of accuracy and efficiency, and it is reasonable to expect considerable improvements.

In this article we first present the structural model of the Grenoble Valley and definition of the numerical simulations. In the next section we briefly introduce the ADER-DGM, FDM, and SEM. Computational aspects of the simulations for the Grenoble Valley are then discussed. The main part of the article presents comparison of the numerical results obtained with the ADER-DGM, FDM, and two implementations of the SEM. We conclude with main lessons learned and recommendations for future blind predictions and benchmark tests.

Structural Model of the Grenoble Valley

Grenoble is settled on Quaternary fluvial and postglacial deposits at the junction of three large valleys of the French external Alps (Fig. 1), surrounded by three mountain ranges. This junction mimics the letter Y (the so-called Grenoble Y), with three legs:

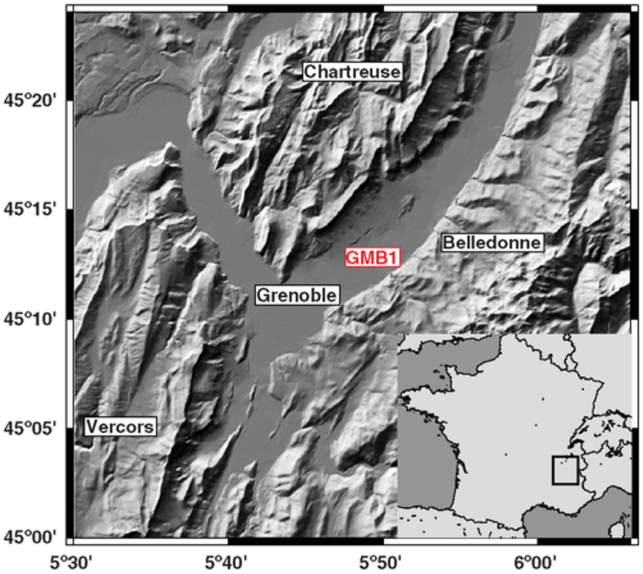

Figure 1. Situation map of the Grenoble area in the French Alps, showing the Y-shaped Grenoble Valley surrounded by the Vercors and Chartreuse limestone massifs with maximal elevation of 2000 m, and the crystalline Belledonne chain where elevation reaches 3000 m. GMB1 indicates the location of the Montbonnot borehole (see text).

1. The northeastern branch of the Y is the N30°–40° trending Grésivaudan Valley, extending about 60 km upstream along the Isère River.
2. The northwestern branch is the N150° trending, Cluse-de-l'Isère Valley, extending from Grenoble to Moirans (about 20 km), where the Isère River flows to the northwest.
3. The southern branch follows the Drac River, flowing from the south and arriving in a small plain about 15 km upstream of Grenoble.

The three massifs delineated by these valleys are the Belledonne crystalline massif to the east and two subalpine foothills consisting of sedimentary rocks (limestone) to the north (Chartreuse) and the southwest (Vercors). These foothills were formed when the Alpine shortening displaced the sedimentary cover to the northwest, forming folds and related thrusts (7 to 5 m.y. B.P.) and uplifted the crystalline basement (5 m.y. B.P.) to the east of the study area (Belledonne massif).

The IsèreValley (from upper Grésivaudan to downstream Cluse-de-l'Isère) therefore extends for about 110 km from Albertville in the northwest to Rovon west of the Vercors massif; it is 3 to 5 km wide and quasi-flat, with slowly decreasing altitudes (330 m in Albertville, 211 m in Grenoble, 180 m in Rovon). The surrounding mountains exhibit, however, a pronounced topography with maximum elevations slightly above 2000 m in Vercors and Chartreuse and above 3000 m in the Belledonne massif. As explained by Gamond *et al.*

(2009), this course runs along several hundred meters deep paleovalley carved in the Mesozoic sedimentary cover of the Alpine foothills. The northeast-southwest Grésivaudan Valley was dug by erosion around 5 m.y. B.P. through the tributaries of the paleo-Isère River, while the northwest-southeast Cluse-de-l'Isère was carved by epigenesis between 5 and 2 m.y. B.P. when the foothills were uplifted.

Its present morphology presents asymmetrical inclined sides and longitudinal moraines typical of glacial valleys. During the last glacial-interglacial cycles, as all valleys in the western Alps, it was successively eroded and overdeepened by thick Alpine glaciers (Isère glacier, local glaciers of the Belledonne massif, Drac-Romanche glacier) feeding large ice lobes at the piedmont and then filled essentially by lake sediments as glaciers were melting and retreating higher up in the catchments during warm phases. In the IsèreValley, both proglacial and deltaic lacustrine sediments completely filled an up to 900 m deep and 100 km long fjordlike basin during the last deglaciation, while only a thin, fluvial sequence formed during our interglacial period (Chapron *et al.*, 2009).

Despite the relatively good mechanical characteristics of these quaternary deposits, the large impedance contrast with the embedding rocks, together with the large embankment ratio, cause huge amplifications as observed by Lebrun *et al.* (2001), Cornou *et al.* (2003a, 2003b), and Cornou *et al.* (2009). A series of geotechnical and geophysical investigations has thus been carried out in the Grenoble area to improve the knowledge of the underground structure. A summary of these investigations can be found in the series of dedicated articles included in Volume 2 of the ESG 2006 proceedings (Chapron *et al.*, 2009; Cornou *et al.*, 2009; Dietrich *et al.*, 2009; Gamond *et al.*, 2009; Guéguen *et al.*, 2009; Jerram *et al.*, 2009; Ménard, Blein, Fournier *et al.*, 2009; Ménard, Dietrich, Vallon *et al.* 2009) and in Guéguen *et al.* (2007). Their primary focus was to constrain the deep structure responsible for the low-frequency effects; once this objective was met, a secondary objective was assigned to better understand the shallow structure controlling the higher-frequency amplification and its short-wavelength lateral variations. Because the ESG 2006 numerical simulations were limited to a 2 Hz maximum frequency, only the deep underground structure and large-scale geometry and topography are presented here.

The first deep investigations consisted in several hundreds of gravimetric measurements that allowed constraining the geometry of the sediment/bedrock interface and indicating a large thickness close to 1 km in the deepest part (Vallon, 1999). This information was checked and calibrated through the drilling of one deep borehole in the Grésivaudan Valley (the Montbonnot GMB1 site in Fig. 1, now instrumented with three accelerometers at the surface, GL-42 m, and GL-550 m), which reached the bedrock at a depth of 535 m, very close to the expectations from the gravimetric survey. Above a thin (4 m thick) glacial till, the post-Würm filling sequence consists in 520 meters of monotonous lacustrine sandy-silty formations corresponding to the postglacial lake, and ends with 15 meters of sandy-pebbly alluvium deposited when the presently working Isère fluviatile regime started again (Nicoud *et al.*, 2002).

As described by Chapron *et al.* (2009), Dietrich *et al.* (2009) and Ménard, Dietrich, Vallon *et al.* (2009), the nature of this postglacial sedimentary infill has also been documented by a set of seismic reflection profiles acquired both on land in the Isère Valley and in large valley lakes, such as the Le Bourget Lake 50 km to the north of Grenoble. All highlight very thick, rather homogeneous quaternary deposits with nonnegligible P- and S-wave velocity gradients. All these measurements have been complemented by several hundreds of microtremor measurements processed with the H/V technique (Guéguen *et al.*, 2007, 2009), which consistently exhibit a low-frequency peak (usually between 0.3 and 0.5 Hz) associated with the thick lacustrine filling, and in some parts, a second higher frequency peak (ranging from 2 to 5–6 Hz).

In summary, the main conclusions of all these deep investigations are:

- 20 km of seismic reflection profiles at different cross sections along the Isère Valley, together with the information collected in the borehole drilled near Grenoble and reaching the sediment-bedrock, allowed us to calibrate or confirm the information provided by gravimetric surveys and background noise H/V measurements on distribution of the sediment thickness in the valley.
- The bottom of the valley is marked by an irregular topography. The bottom of the Isère Valley shows a great variety of shapes: flat bottom, wide open V-shape, V-shape interlocked in a larger U-shaped valley. At some places, there exist underground substratum highs, such as a hillock (probably of tithonic age) that could be identified just south of the Grenoble downtown (see Fig. 2).
- The depth of the substratum increases downstream the Isère River from about 200 m in the upper Grésivaudan, 500 m in the lower Grésivaudan, and more than 800 m in the Cluse of Grenoble.
- The seismic velocities are roughly laterally homogeneous at depths larger than 20–40 m, in line with the filling of the valley by the postglacial lacustrine deposits.
- The P- and S-wave velocity distributions within the sediments are characterized by moderate to strong vertical gradients, with the V_P/V_S ratio varying between 6 near the surface and 2.7 at several hundred meters depth.

Given the limitation of our numerical simulation exercise to an upper frequency of 2 Hz, we thus considered a simple depth-varying sediment velocity model derived from the deep borehole measurements. The valley model is thus described by two main components:

- A 3D geometry consisting of a free-surface topography and a sediment-basement interface.
- Sediment and bedrock velocity models exhibiting only a 1D depth dependence.

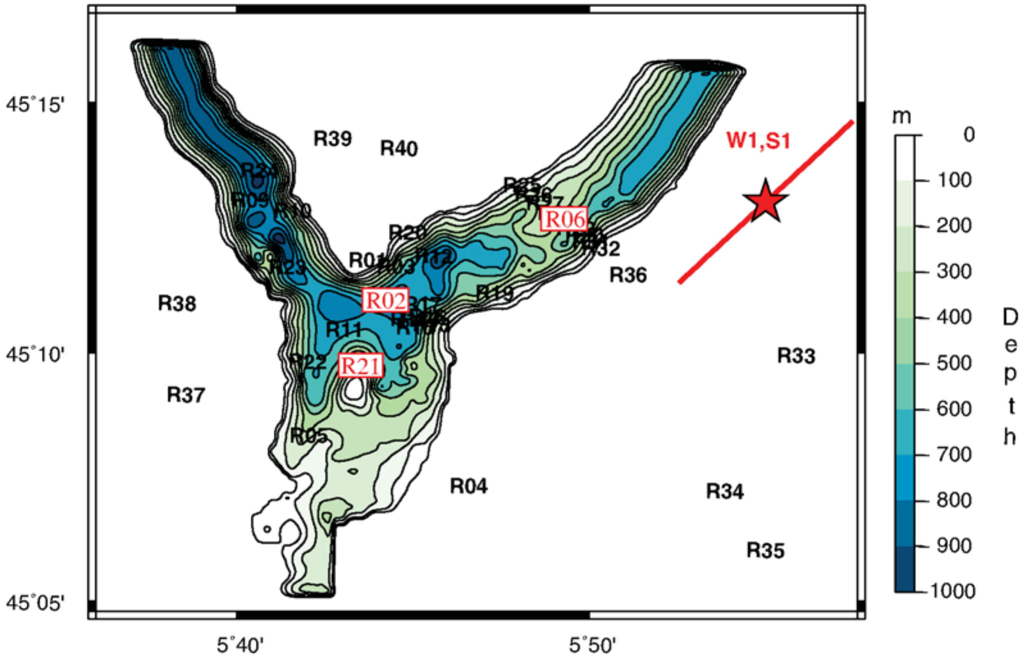

Figure 2. Map of sediment thickness in the Grenoble Valley showing 40 receivers (R01 to R40) used in the simulations. Contour lines every 100 m are shown; the bold black line indicates the points where the sediment thickness equals 50 m. The positions of the point source W1 and extended source S1 are shown in red. Red boxes indicate particular receivers for which a detailed comparison is shown further in the article. Receiver R06 corresponds to the GMB1 location in Figure 1.

The geometry of the surface topography is shown in Figure 1, and the underground topography is depicted in Figure 2. The velocity model is detailed in Table 1. This model is still distant from the reality, especially for the shallow part. It constitutes, however, a good starting model that is able to reproduce the main features of the low-frequency response, and it is complex enough to enable a meaningful comparison between different numerical methods.

The quality factor values were chosen infinite in the underlying bedrock. The bedrock is very stiff and the computations are performed only for local, shallow sources, so that crustal damping effects may be thought negligible in a first step. The quality factor was taken slightly larger than that actually measured in the Montbonnot borehole ($Q_P = 35$, see Cornou, 2002), but these measurements were obtained at higher frequencies (several tens of Hertz); higher Q values are needed to reproduce the observed low-frequency duration within the valley (Chaljub, 2009).

Selected Earthquakes

Various active tectonic features such as basement thrusts and strike-slip faults have been described in this part of the Alps (Thouvenot *et al.*, 2003, 2009). However, the known history reports only moderate earthquakes with intensities reaching VIII on the Medvedev, Sponheuer, and Karnik (MSK) scale, and estimated magnitudes between *M* 5 and *M* 6. The last significant earthquake in the Grenoble immediate surroundings was an *M* 5.3 earthquake that occurred in Corrençon (Vercors, about 30 km to the southwest of Grenoble) in 1962, which caused some chimney falls in the city.

The densification of the seismic monitoring networks undertaken in the late 1980s revealed some clear, previously unsuspected seismic alignments. In particular, the Belledonne Border Fault (BBF) has been identified as the most active of these new features: it consists of a 50 to 70 km long, northeast-southwest trending segment, characterized by

Table 1

Mechanical Parameters for the Grenoble Valley Model

Unit	Thickness	Unit Mass (kg/m^3)	*S*-Wave Velocity β (m/sec)	*P*-Wave Velocity α (m/sec)	Quality Factor Q_S	Quality Factor Q_P
Sediments	Up to 1000 m	$2140 + 0.125z$*	$300 + 19\sqrt{z}$	$1450 + 1.2z$	50	$37.5\ \alpha^2/\beta^2$
Bedrock	0–3 km	2720	3200	5600	∞	∞
	3–27 km	2720	3430	5920	∞	∞
	27–35 km	2920	3810	6600	∞	∞
	> 35 m	3320	4450	8000	∞	∞

*z refers to depth expressed in meters.

many small earthquakes exhibiting a right-lateral strike-slip motion consistent with an east–west compressive tectonic environment. Such a segment could therefore easily accommodate an *M* 6 event, with recurrence rates, however, well beyond the 500- to 1000-year historic period. This fault runs indeed east of and parallel to the northeast branch of the Y, with a distance of approximately 5–7 km from the eastern edge of the Isère–Grésivaudan Valley.

Because several recordings could be obtained at different sites from a small magnitude event on this fault near the village of Lancey in 2003, it was decided to simulate the ground motion for two earthquakes (Chaljub *et al.*, 2009):

- A real, weak one, called W1, corresponding to this 2003 event. This event had a moment magnitude *M* 2.9, and was assumed to be a point source with a 45° strike angle and a 90° dip angle, located at a 3 km depth. (There is, however, a significant uncertainty on the depth estimate, which could be up to 8 km).
- A hypothetical, stronger event (S1), corresponding to an *M* 6 event rupturing the Belledonne Border Fault along a segment centered at the W1 hypocenter. The fault length and width were assumed to be 9 and 4.5 km, respectively. A very simple (and, indeed, somewhat pessimistic and unrealistic) kinematics was assumed. The rupture nucleates at the fault center, propagates circularly with a rupture velocity equal to 2.8 km/sec, and stops abruptly when it reaches the boundary of the rectangular fault area. In addition, the slip distribution is flat (i.e., constant slip over the whole ruptured area). Such a fault mechanism generates very strong stopping phases, especially as the rupture is very shallow: the resulting ground-motion values are thus unrealistically high, and should be taken with much caution if applied to hazard estimates. Such a scenario nevertheless constitutes a good case for a comparison between different numerical methods, because it includes very strong pulses with high directivity.

For both cases, the source function was defined as

$$s(t) = 0.5(1 + \mathrm{erf}[4(t - 2\tau)/\tau]), \tag{1}$$

where τ is the rise time chosen to provide an average slip velocity on the fault plane equal to 1 m/sec. It was thus taken equal to 0.03 sec for the weak event (W1) case, and to 1.16 sec for the strong event case (S1).

The ground motion from each of these events was computed at a series of 40 receivers displayed in Figure 2 (some of them corresponding to the location of a few seismological or accelerometric stations that recorded the *M* 2.9, 2003 Lancey earthquake). Most of these receivers are located at the surface, but two are located at depth and correspond to the Montbonnot downhole sensors (receiver R06 corresponds to the GMB1 location in Fig. 1). Receivers R01, R04, and R33 to R40 are located on rock outcrops, whereas all the others are located within the valley.

The simulation exercise proposed for the ESG 2006 symposium also included another set of twin events (W2, S2), located 20 km to the south of Grenoble, corresponding to a conjugate strike-slip fault with a west-northwest–east-southeast strike. A more complete description of the simulation exercise can be found in Chaljub *et al.* (2009) and Tsuno *et al.* (2009). In the present article, however, only the (W1, S1) set of events is considered.

Fourteen different groups from eight countries contributed to the ESG 2006 comparison, providing a total of 18 prediction sets; three groups used the empirical Green's function technique for the few receivers collocated with strong motion stations, two used a 1D (horizontal layering) approach for the borehole site, three modeled the response of a 2D cross section, and seven addressed the 3D problem, out of which three could account for the effects of both underground and surface topography. The numerical schemes used for 3D contributions belong to the finite-difference, spectral-element and discontinuous-Galerkin finite-element methods. Four participants whose 3D predictions were surprisingly close updated their results after the ESG meeting, after correcting some nonmethodological errors (evidenced by comparing to other predictions) in preparation of the numerical simulations. Only the results from the corrected predictions are considered here. Further details on all other methods and results can be found in Tsuno *et al.* (2009).

Computational Methods

3D Fourth-Order Velocity-Stress Finite-Difference Scheme on an Arbitrary Discontinuous Staggered Grid

Although the FDM has been used in seismology since the late 1960s, its elaboration for the structurally complex media is certainly far from being completed. Recent elaboration of the staggered-grid schemes for viscoelastic media with material interfaces as well as the development of the optimally accurate schemes are two examples soundly indicating that the best times of the finite-difference modeling are still ahead of us. Because we do not have space here for more details, we refer to the recent comprehensive review (Moczo, Robertsson, Eisner, 2007) and monograph (Moczo *et al.*, 2007).

For the numerical simulations we used a 3D fourth-order velocity-stress finite-difference scheme on an arbitrary discontinuous staggered grid. A complete theory can be found in articles by Moczo *et al.* (2002, 2004), Kristek *et al.* (2002), Kristek and Moczo (2003), and Moczo and Kristek (2005). Here we restrict our focus to the essential aspects of the simulation method.

The scheme solves the equation of motion and Hooke's law for viscoelastic medium with rheology of the generalized Maxwell body,

$$\rho \dot{v}_i = \sigma_{ij},_j + f_i, \tag{2}$$

and

$$\dot{\sigma}_{i,j} = \kappa\dot{\varepsilon}_{kk}\delta_{ij} + 2\mu\left(\dot{\varepsilon}_{ij} - \frac{1}{3}\dot{\varepsilon}_{kk}\delta_{ij}\right) - \sum_{l}^{4}\left[\kappa Y_l^{\kappa}\xi_l^{kk}\delta_{ij} + 2\mu Y_l^{\mu}\left(\xi_l^{ij} - \frac{1}{3}\xi_l^{kk}\delta_{ij}\right)\right], \quad (3)$$

$$\dot{\xi}_l^{ij} + \omega_l\xi_l^{ij} = \omega_l\dot{\varepsilon}_{ij}; \qquad l = 1, \ldots, 4. \quad (4)$$

Here, in a Cartesian coordinate system (x_1, x_2, x_3), $\rho(x_i)$; $i\in\{1,2,3\}$, is density; $\kappa(x_i)$ and $\mu(x_i)$ unrelaxed (elastic) bulk and shear moduli; Y_l^{κ} and Y_l^{μ} anelastic coefficients; $\vec{u}(x_i, t)$ displacement vector; t time; $\vec{f}(x_i, t)$ body force per unit volume; $\sigma_{ij}(x_k, t)$, $\varepsilon_{ij}(x_k, t)$, i, j, and $k\in\{1,2,3\}$ stress and strain tensors; ξ_l^{ij} material-independent anelastic functions; and ω_l relaxation angular frequencies. Summation convention does not apply to index l. The anelastic coefficients are obtained from

$$Y_l^{\kappa} = \left(\alpha^2 Y_l^{\alpha} - \frac{4}{3}\beta^2 Y_l^{\beta}\right)\Big/\left(\alpha^2 - \frac{4}{3}\beta^2\right),$$
$$Y_l^{\mu} = Y_l^{\beta}; \qquad l = 1, \ldots, 4, \quad (5)$$

where α and β are elastic (corresponding to the unrelaxed moduli) *P*- and *S*-wave velocities, and anelastic coefficients Y_l^{α} and Y_l^{β} are obtained from the desired/measured quality factor values

$$Q_{\nu}^{-1}(\tilde{\omega}_k) = \sum_{l=1}^{n}\frac{\omega_l\tilde{\omega}_k + \omega_l^2 Q_{\nu}^{-1}(\tilde{\omega}_k)}{\omega_l^2 + \tilde{\omega}_k^2}Y_l^{\nu};$$
$$k = 1, \ldots, 7, \qquad \nu\in\{\alpha, \beta\}. \quad (6)$$

The schemes for solving the equation of motion and time derivative of Hooke's law have the same structure as standard fourth-order velocity staggered-grid schemes. The accuracy of our scheme is determined by how we treat smooth material heterogeneity and material discontinuity. The effective grid density for a corresponding particle velocity component is evaluated as an integral volume arithmetic average of density inside a grid cell centered at the grid position of the corresponding particle velocity component; for example

$$\rho^{A}_{I,J+1/2,K+1/2} = \frac{1}{h^3}\int_{x_{I-1/2}}^{x_{I+1/2}}\int_{y_J}^{y_{J+1}}\int_{z_K}^{z_{K+1}}\rho\,\mathrm{d}x\mathrm{d}y\mathrm{d}z. \quad (7)$$

The effective grid, unrelaxed bulk, and shear moduli are evaluated as integral volume harmonic averages of moduli in respective grid cells centered at grid positions of the stress-tensor components; for example

$$\kappa^{H}_{I+1/2,J+1/2,K+1/2} = \left[\frac{1}{h^3}\int_{x_I}^{x_{I+1}}\int_{y_J}^{y_{J+1}}\int_{z_K}^{z_{K+1}}\frac{1}{\kappa}\mathrm{d}x\mathrm{d}y\mathrm{d}z\right]^{-1}. \quad (8)$$

The integrals are evaluated numerically, and the grid cell can contain a material discontinuity. The anelastic coefficients Y_l^{κ} and Y_l^{μ} are determined as follows: An average viscoelastic modulus in the frequency domain is numerically determined for a cell as an integral harmonic average. A corresponding quality factor is then determined from the averaged viscoelastic modulus at specified frequencies. Equation (6) for the bulk and shear moduli is then used to determine average anelastic functions. A coarse spatial distribution of the anelastic functions is applied in order to reduce the memory requirements.

The free surface is simulated using the AFDA technique (Kristek *et al.*, 2002; Moczo *et al.*, 2004).

If the near-surface sedimentary body with lower seismic wave velocities is covered by a fine spatial grid and underlying stiffer bedrock with larger velocities is covered by a coarser spatial grid, the number of grid points and, consequently, the computer memory and time requirements are significantly reduced compared with the uniform grid. In order to make such a combined (or discontinuous) spatial grid efficient, the ratio of the size of the spatial grid spacing in the coarser grid and that in the finer grid should correspond to the ratio of the shear-wave velocities in the stiffer bedrock and softer sediments. Therefore, Kristek *et al.* (2009) and Moczo *et al.* (2007) developed an algorithm that enables us to adjust a discontinuous spatial grid accordingly except that, due to the structure of the staggered grid, the ratio of the spatial grid spacings in the coarser and finer grids has to be an odd number. In other words, depending on the model of medium, we can choose a 1:1 (uniform) grid, or 1:3, 1:5, … discontinuous grid. The grid is illustrated in Figure 3. A Fortran 95 computer code 3DFD_VS has been developed for performing the finite-difference scheme. PML absorbing boundary conditions are implemented. The code is MPI parallelized (see the Data and Resources section for details).

3D Spectral-Element Method

The spectral-element method (SEM) has been introduced quite recently for seismological applications (Seriani and Priolo, 1991, 1994; Faccioli *et al.*, 1997; Komatitsch and Vilotte, 1998). The SEM is a special kind of the finite-element method (FEM) that relies on the use of a high-order spectral polynomial basis. Like the FEM, the SEM can naturally handle media with complex geometries, including surface topography and nonplanar interfaces, and it allows local mesh refinement to account for variations in seismic wavelengths. Moreover, compared with the traditional low-order FEM, the high-order spectral basis yields very accurate results by minimizing numerical dispersion and numerical anisotropy (Seriani and Oliveira, 2007; de Basabe and Sen, 2007). In practice, polynomial orders $N = 4$ to $N = 8$ are used and provide sufficiently accurate results for both body and surface waves, as soon as 5 to 6 points are used to sample the seismic wavelengths.

In the classical SEM, as in the two implementations presented hereafter, the choice of the element shapes, polynomial basis, and numerical integration rule relies on tensorization, that is, on separation of variables. The advantage is the possibility to increase significantly the computational

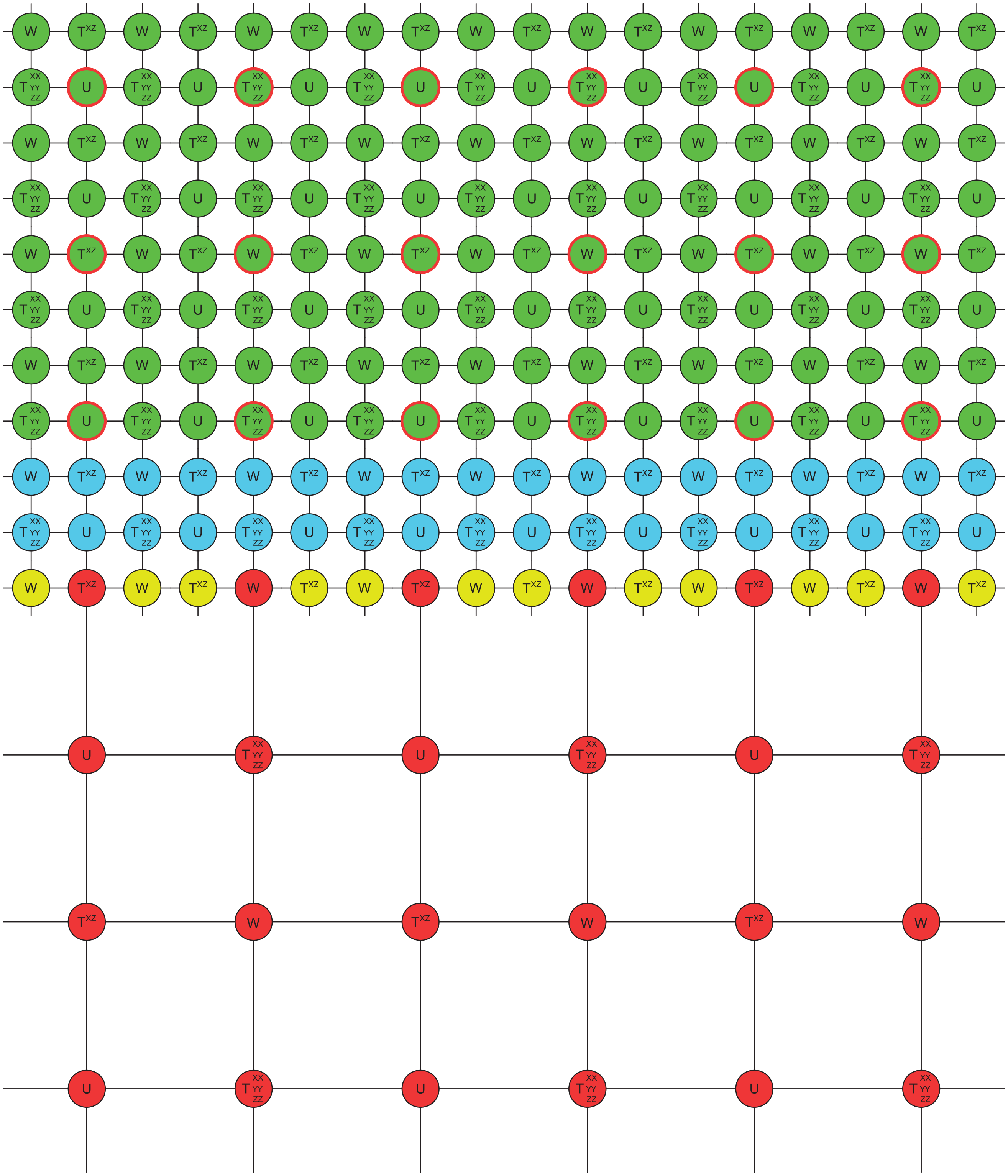

Figure 3. A vertical grid plane in the arbitrary discontinuous spatial staggered grid in the case of the coarser-to-finer spatial grid spacing equal to 3. The interior grid positions of the finer grid: green, 4th-order FD scheme; blue, 2nd-order FD scheme; yellow, bicubic interpolation. The interior grid positions of the coarser grid: red, 4th-order FD scheme. The red-circumscribed green positions define the boundary of the coarser grid.

efficiency by (1) leading to a diagonal mass matrix, allowing fully explicit schemes to be used for time evolution; and (2) decreasing the computational cost of the internal forces. The drawback is the restriction of the geometry of spectral elements to quadrangles in 2D and to hexahedra in 3D. Recall indeed that in order to account properly for discontinuities in elastic parameters, the spectral elements must not intersect the physical interfaces. This condition is not always easy to account for in a hexahedra-based SEM, for example, near valley or basin edges. Extensions of the SEM to 2D meshes of triangular elements have been proposed recently at the price of either losing the diagonal character of the mass matrix (Mercerat *et al.*, 2005) or decreasing the spectral accuracy (Komatitsch *et al.*, 2001).

Review papers presenting the numerous developments of the SEM for global or regional seismology applications can be found in Komatitsch *et al.* (2005) and Chaljub *et al.* (2007). Here, we briefly recall the key features of the SEM discretization.

Through the principle of virtual work, the dynamic equilibrium problem for the medium Ω can be stated in the following weak or variational form: find $\boldsymbol{u} = \boldsymbol{u}(\boldsymbol{x}, t)$, displacement vector, such that $\forall t \in (0, T)$

$$\frac{\partial^2}{\partial t^2}\int_{\Omega}\rho\boldsymbol{u}\cdot\boldsymbol{v}d\Omega+\int_{\Omega}\sigma_{ij}(\boldsymbol{u})\varepsilon_{ij}(\boldsymbol{v})d\Omega = \int_{\Gamma_N}\boldsymbol{t}\cdot\boldsymbol{v}d\Gamma+\int_{\Omega}\boldsymbol{f}\cdot\boldsymbol{v}d\Omega, \quad i,j=1\ldots d \quad \text{for all } \boldsymbol{v}, \tag{9}$$

where t is time, $\rho = \rho(\boldsymbol{x})$ the material density, σ_{ij} the stress-tensor, ε_{ij} the infinitesimal strain tensor, $\boldsymbol{f} = \boldsymbol{f}(\boldsymbol{x}, t)$ the known body force distribution, $\boldsymbol{t} = \boldsymbol{t}(\boldsymbol{x}, t)$ the vector of external traction prescribed on Γ_N, and $\boldsymbol{v} = \boldsymbol{v}(x)$ is the generic function (candidate to represent admissible displacements). Note that the free-surface condition is obtained implicitly, or naturally, in the weak formulation. The stress and strain tensors in (9) are related to the displacement by Hooke's law (3).

An appropriate numerical solution of (9) can be achieved through discretization in the space and time domain. Herein, the latter is done via finite differences; the best trade-off in terms of accuracy, stability, and computational complexity is obtained using the explicit second-order leapfrog scheme (LF2-LF2) (Maggio and Quarteroni, 1994) that must satisfy the well-known Courant-Friedrichs-Lewy (CFL) stability condition.

The spatial discretization is based upon the Galerkin approximation to equation (9). It starts with a decomposition of the computational domain Ω into a family of nonoverlapping, unstructured quadrilaterals Ω_k (or hexahedra in 3D). Each element Ω_k is obtained by a regular mapping of a reference element Ω_{ref} (the unit square $[-1,+1]^2$ in 2D and the unit cube $[-1,+1]^3$ in 3D). Then, admissible displacements are approximated by polynomials of degree N on each element. This writes formally

$$\sum_{k=1}^{K}\frac{\partial^2}{\partial t^2}\int_{\Omega_k}\rho u_N^{(i)}\cdot v^{(i)}d\Omega+\sum_{k=1}^{K}\int_{\Omega_k}\sigma_{lm}(\boldsymbol{u}_N^{(i)})\varepsilon_{lm}(\boldsymbol{v}_N^{(i)})d\Omega = \sum_{k=1}^{K}\int_{\Gamma_N^{(k)}}t^{(i)}v^{(i)}d\Gamma_N+\sum_{k=1}^{K}\int_{\Omega_k}f^{(i)}v^{(i)}d\Omega, \tag{10}$$

where $\boldsymbol{u}_N$ and $\boldsymbol{v}_N$ denote the approximations of $\boldsymbol{u}$ and $\boldsymbol{v}$, and $u_N^{(i)}, v_N^{(i)}, t_N^{(i)}, f^{(i)}$ the scalar components of the vectors $\boldsymbol{u}_N, \boldsymbol{v}_N$, $\boldsymbol{t}$ and $\boldsymbol{f}$. Note that equation (10) implicitly assumes that the displacements are globally continuous, but the material properties can be discontinuous across elements.

The integrals in (10) are evaluated numerically by a high-order quadrature formula based on the Gauss-Lobatto-Legendre (GLL) points (Davis and Rabinowitz, 1984; Canuto *et al.*, 1988). The polynomials used to approximate the displacements are then defined as the shape functions of the GLL points. Thanks to this particular choice, the SEM inherits the exponential accuracy of spectral methods in space: for problems with sufficiently smooth exact solution $\boldsymbol{u}$, the numerical solution $\boldsymbol{u}_N$ obtained in the SEM converges more rapidly than those based upon the classical FEM. This property is known as spectral accuracy in the literature, and the convergence of the spectral methods is referred to as exponential or geometrical, as opposed to the algebraic convergence of the classical FEM. Note that this does not hold for the numerical realization of the free-surface condition: the convergence of numerical traction toward the prescribed traction is only algebraical (Deville *et al.*, 2002). For the wave propagation applications, the numerical accuracy is more properly assessed by the analysis of numerical dispersion, which has been shown recently to be optimal for the SEM (Seriani and Oliveira, 2007; de Basabe and Sen, 2007).

Assembling the elementary contributions to account for the continuity of displacements, equation (10) can be written as a global system of ordinary differential equations in time,

$$[M]\ddot{\boldsymbol{U}}(t)+[K]\boldsymbol{U}(t)=\boldsymbol{F}(t)+\boldsymbol{T}(t), \tag{11}$$

where vectors $\boldsymbol{F}$ and $\boldsymbol{T}$ stem from the contributions of the external forces and applied tractions, $\boldsymbol{U}$ stores the displacement values $\boldsymbol{u}_N(x,t)$ at the GLL nodes, and $[M]$ and $[K]$ denote the mass and the stiffness matrices, respectively. An important consequence of the choice of the polynomial basis is that the mass matrix is diagonal, which, as stated previously, allows for the use of fully explicit finite-difference schemes for the time evolution.

In the following we will present two different implementations of the SEM. In the first SEM-based code, hereafter referred to as SEM1, viscoelasticity is accounted for using a superposition of the standard linear solids (SLS; Liu *et al.*, 1976), which are implemented via memory variables (see Chaljub *et al.*, 2007, and references therein). Note that a parallel superposition of the SLS is also called the generalized Zener body. Also note that the rheology of the generalized Zener body is equivalent to that of the generalized Maxwell body as shown by Moczo and Kristek (2005). Thus, the rheology in the SEM1 is equivalent to that implemented in the FD and ADER-DGM methods described in the article. The Lysmer and Kuhlemeyer (1969) absorbing boundary conditions are applied. (See the Data and Resources section for details on the SEM1 software package.)

In the second implementation, hereafter referred to as SEM2, the viscoelastic behavior is implemented with a frequency linear dependent quality factor, implying that all frequency components are equally attenuated (Faccioli *et al.*, 1997). Kosloff and Kosloff (1986) showed that this can be easily obtained by replacing the inertia term into the wave equation with an *ad hoc* expression. The absorbing boundaries are implemented following Stacey's (1988) first-order P3 paraxial conditions. A more detailed description of the software package adopted for the SEM2 simulation can be found in Stupazzini *et al.* (2009) (also see the Data and Resources section for details on the SEM2 software).

3D Velocity-Stress Discontinuous Galerkin Scheme with ADER-Time Integration of Unstructured Tetrahedral Meshes

The proposed numerical method combines a discontinuous Galerkin (DG) finite-element scheme with a time-integration technique using Arbitrarily high-order DERivatives (ADER) in order to solve the governing PDE with arbitrarily high approximation order in time and space. The system of the 3D seismic wave equations formulated in velocity-stress leads to a hyperbolic system of the form

$$\frac{\partial Q_p}{\partial t} + A_{pq}\frac{\partial Q_q}{\partial \xi} + B_{pq}\frac{\partial Q_q}{\partial \eta} + C_{pq}\frac{\partial Q_q}{\partial \zeta} = E_{pq}Qq + S_p, \tag{12}$$

where the vector Q of unknowns contains the six stress and the three velocity components. The Jacobian matrices A, B, and C include the material values and can include anisotropic, viscoelastic, or poroelastic material properties as explained in detail in Dumbser and Käser (2006), Käser *et al.* (2007), de la Puente *et al.* (2007) and (2008). The viscoelastic medium and the attenuation is defined by rheology of the GMB-EK, the same as described in the section on the finite-difference method. Furthermore, the reactive source term E is necessary, if viscoelastic attenuation is considered, and S is an external source term accommodating force of moment tensor sources. In the discontinuous Galerkin approach, the solution is approximated inside each tetrahedral element by a linear combination of space-dependent polynomial basis functions and time-dependent degrees of freedom as expressed through

$$(Q_h)_p(\xi,\eta,\zeta,t) = \hat{Q}_{pl}(t)\Phi_l(\xi,\eta,\zeta), \tag{13}$$

where the basis functions Φ_l form an orthogonal modal basis and are defined on the canonical reference tetrahedron. Note that there are no integration points necessary, because the basis is a modal basis and not a nodal basis as typically used in the SEM.

As the fully detailed derivation of the numerical scheme would go beyond the scope of this article, we refer to the previous work of Käser and Dumbser (2006) and Dumbser and Käser (2006) for a detailed mathematical formulation of the discontinuous Galerkin method. The unique property of the ADER-DGM scheme is, that the time accuracy of the scheme is automatically coupled to the space accuracy determined by the degree of approximation polynomials used in equation (13). This is due to the ADER time-integration approach (Titarev and Toro, 2002), where the fundamental idea is to expand the solution of equation (12) via a Taylor series in time

$$Q_p(\xi,\eta,\zeta,t) = \sum_{k=0}^{N}\frac{t^k}{k!}\frac{\partial^k}{\partial t^k}Q_p(\xi,\eta,\zeta,0), \tag{14}$$

where we then replace all time derivatives in equation (14) by space derivatives using the governing PDE in equation (12). It can be shown that the k-th time derivative can be expressed recursively as

$$\begin{aligned}\frac{\partial^k}{\partial t^k}Q_p = (-1)^k\left(A_{pq}\frac{\partial}{\partial \xi} + B_{pq}\frac{\partial}{\partial \eta} + C_{pq}\frac{\partial}{\partial \zeta}\right)^k Q_q \\ + E_{pq}\frac{\partial^{k-1}}{\partial t^{k-1}}Q_p + \frac{\partial^{k-1}}{\partial t^{k-1}}S_p.\end{aligned} \tag{15}$$

Using equations (13) and (15) in (14), the Taylor series expansion only depends on space derivatives of the basis functions Φ_l and lower order time derivatives of the source terms. The resulting expression for the degrees of freedom can be integrated in time analytically as shown in detail by Dumbser and Käser (2006) or Käser *et al.* (2007). Therefore, this new approach, termed ADER-DG method, provides arbitrarily high-order approximation in space and time depends on the degree of the used basis polynomials Φ_l in equation (13) and the corresponding order of the time Taylor series chosen in equation (14).

Once the high-order time-integrated degrees of freedom are computed, the evolution of the numerical solution in time is calculated via local stiffness and flux terms (Dumbser and Käser, 2006). Especially, the flux computations contribute as the major part with more than 80% to the overall computational cost. A numerical flux out of the element and a numerical flux into the element have to be calculated for each element boundary, that is, triangular surface, for each tetrahedral element. Each flux computation requires a multiplication of two matrices F and Q of the sizes:

size of F: (number of degrees of freedom) × (number of degrees of freedom) and

size of Q: (number of degrees of freedom) × (number of variables in the system).

The stiffness terms, however, are relatively cheap as only one matrix-matrix-multiplication of the same computational complexity has to be carried out. Nevertheless, all operations use only local data, that is, data from the element itself and its direct neighbor sharing a common element boundary. Due to this local character of the numerical scheme, a number of different optimization approaches have been developed (Dumbser *et al.*, 2007) to enhance computational efficiency, in particular for parallel computing.

p_τ-Adaptation. In most applications, the computational domain is larger than a particular zone of interest. Therefore, a large number of elements is needed to discretize the entire geometry of the model. However, high-order accuracy might only be required in a relatively small portion of the computational domain, which makes it desirable to choose the accuracy adaptively in space. With the ADER-DG approach, it is possible to vary the degree p of the approximation polynomials Φ_l in equation (13) from one element to the other. Due to the direct coupling of the time and space accuracy via the ADER approach, the scheme automatically becomes adaptive in time accuracy, which is referred to as p_τ-adaptation.

Local Timestepping. Geometrically complex computational domains or spatial resolution requirements often lead to meshes with small or possibly degenerate elements. The timestep for explicit numerical schemes is determined by the ratio of the mesh size h of the smallest element and the corresponding maximum wave speed in this element. For global timestepping schemes, all elements are updated with this extremely restrictive timestep length, leading to a large amount of iterations. With the ADER approach, time accurate local timestepping can be used, so that each element is updated by its own, optimal timestep. An element can be updated to the next time level if its actual time level and its local timestep Δt fulfill the condition with respect to all neighboring tetrahedrons n,

$$t + \Delta t \leq \min(t_n + \Delta t_n). \tag{16}$$

Information exchange between elements across interfaces appears when numerical fluxes are calculated. These fluxes depend on the length of the local time interval over which a flux is integrated and the corresponding element is evolved in time. Therefore, when the update criterion (16) is fulfilled for an element, the flux between the element itself and its neighbor n has to be computed over the local time interval:

$$\tau_n = [\max(t, t_n), \min(t + \Delta t, t_n + \Delta t_n)]. \tag{17}$$

This can reduce the overall amount of flux calculations dramatically because only the small elements have to be updated frequently according to their small timestep lengths. A full description of the p_τ-adaptation and local timestepping of the ADER-DG scheme is given by Dumbser *et al.* (2007).

Grouped Mesh Partitioning. For large-scale applications it is essential to design a parallel code for supercomputing facilities, where load balancing is an important issue. However, if p_τ-adaptivity and especially local timestepping are applied, the partitioning is sophisticated because a subdomain can have different polynomial orders and timestep lengths. We split the computational domain into zones that usually contain geometrical or geological entities that are meshed individually. Then, each of these zones is partitioned separately into subdomains of equal numbers of elements, which now include tetrahedral elements with roughly the same sizes and orders of accuracy. Finally, each processor receives a subdomain from each zone and therefore gets a similar computational load. In Figure 4a we show a partition of the full tetrahedral mesh used for the Grenoble model, where each subdomain is color-coded. In Figure 4b we show the grouped partitioning used to improve load balance.

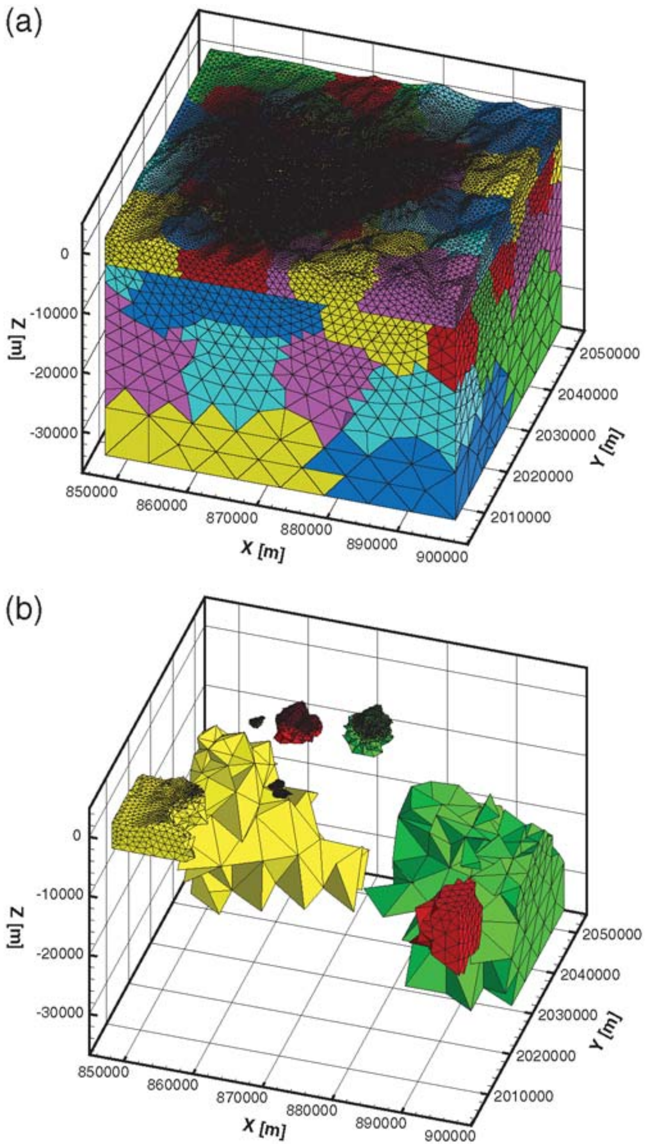

Figure 4. (a) Partitioning of an unstructured tetrahedral discretization of the Grenoble model. (b) Separate subdomains that contain a balanced number of small and large tetrahedrons from different zones are given to each processor, as indicated by the same color, to optimize the load balance.

Comparison of Computational Aspects in Modeling Earthquake Motion in Grenoble Basin

3D Fourth-Order Velocity-Stress Finite-Difference Scheme on an Arbitrary Discontinuous Staggered Grid

Space-Time Grid. The computational domain is a rectangular parallelepiped covered by a discontinuous staggered grid. The upper part of the model with a sedimentary body, 1125 m thick, is covered by a finer grid with a grid spacing of 25 m. The finer grid is made of 1321 × 1431 × 45 grid cells. The lower part of the model, covering a major part of the bedrock, 8125 m thick, is covered by a coarser grid with a grid spacing of 125 m. The coarser grid is made of 265 × 287 × 65 grid cells. The coarser grid is overlapping 187.5 m of the finer grid. The 1:5 discontinuous spatial grid means 87% reduction in the total number of grid cells compared to the uniform grid with a grid spacing of 25 m (approximately 90 mil. of grid cells in the discontinuous grid instead of 700 mil. of grid cells in the uniform grid). Fifty and ten grid spacings are grid thicknesses of the PML boundary regions in the finer and coarser grids, respectively. The timestep is 0.0022 sec. The used spatial grid means that the simulation should be sufficiently accurate up to 2.5 Hz.

Material Heterogeneity and Attenuation. The true model geometry of the material interfaces as well as the smooth material heterogeneity inside the sedimentary body are accounted for in the evaluation of the effective material elastic and anelastic grid parameters grid using relations (5)–(8) and the approach described therein. We can note that the scheme using the integral volume harmonic averages of the moduli and integral volume arithmetic average of density, evaluated for each cell centered at a relevant grid position, is capable to sense the true position of the material interfaces within the cell.

The constant $Q(\omega)$ law is simulated using the rheology of the generalized Maxwell body. The so-called coarse grid graining is applied in the spatial discretization of the anelastic coefficients and functions. The Q values are specified at four frequencies: 0.07 Hz, 0.225 Hz, 0.71 Hz, and 2.25 Hz. This should accurately cover the frequency range of 0.04 to 4 Hz. The P- and S-wave velocities are specified at a frequency of 1 Hz.

Treatment of the Kinematic Source. The finite kinematic model of the rupturing surface is simulated using 1836 regularly distributed point double-couple sources over a fault area 9 km × 4.5 km for the S1 event. Each point source is simulated using a discrete system of body forces acting at the grid positions centered at the grid position of the normal stress-tensor component. All point sources have the same focal parameters and source-time functions. The action of the individual point sources in time is prescribed and corresponds to the specified rupture velocity.

Accuracy versus Efficiency. All simulations were performed on a small cluster of the Opteron 2.2 machines (6 CPUs, 10 GB RAM in total). The computational parameters are given in Table 2.

3D Spectral-Element Method: The SEM1 Implementation

Model Geometry and Mesh Generation. In the first implementation of the SEM, SEM1, a simple meshing strategy, as proposed by Komatitsch *et al.* (2004), is adopted. The topology of the mesh is that of a layer-cake model in which the interfaces are deformed to follow, as much as possible, the physical interfaces. This strategy has the advantage of being easy to implement, but it also has some drawbacks. First, the size of the elements does not vary horizontally, which prevents the use of very large models as the ones that would be needed to propagate the seismic wave field from a distant earthquake to the Grenoble Valley. For the Grenoble simulation, which considers only local sources, this point is not critical; it has the nice consequence of providing a more accurate discretization of the free-surface topography, which is rather stiff in the Grenoble area (see Fig. 5). Second, the sediment-bedrock interface is not accounted for at depths shallower than about 350 m (see Fig. 6). The velocity

Table 2

Comparison of the Computational Parameters

Test Case	Number of Grid Cells or Elements	Order in Space/Time	Timestep	Number of Central Processing Units	Central Processing Unit Time	Memory
DSG Velocity-Stress FD						
W1 Flat	90,009,370	4/2	0.0022 sec	6	~33 hr	~10 GB
S1 Flat	90,009,370	4/2	0.0022 sec	6	~33 hr	~10 GB
SEM1						
W1 Flat	332,160	4/2	0.0005 sec	32	~9 hr	~10 GB
S1 Topography	332,160	4/2	0.0005 sec	32	~9 hr	~10 GB
SEM2						
S1 Topography	216,972	3/2	0.0003 sec	63	~10 hr	~18 GB
ADER-DG						
W1, S1 Flat	870,613	5/5	0.0001 sec	510	~32 hr	~50 GB
S1 Topography	1,259,721	5/5	0.0001 sec	510	~48 hr	~70 GB

contrasts near the valley edges are thus approximated by continuous variations using the polynomial basis within each spectral element. Although not quantified, the error due to this approximation is not expected to be too large because the size of the near-surface elements close to the valley edges is that of the smallest wavelength in the simulation (that is, about 150 m for a 2 Hz calculation). The mesh is coarsened with depth using the conforming strategy proposed by Komatitsch *et al.* (2004) as shown in Figure 6. We use a polynomial order $N = 4$ within each element. For calculations accurate for frequencies up to 2 Hz, the mesh contains 332,160 elements and 22,062,624 grid points.

Material Heterogeneity and Attenuation. For the attenuation model provided in the ESG exercise, the generalized Zener body with three relaxation mechanisms was used in order to mimic a constant shear quality factor in the sediments within the frequency band (0.2 Hz–10 Hz). The reference frequency, which was not imposed, is chosen to be the fundamental frequency of the Grenoble Valley, $f0 = 0.3$ Hz. Time extrapolation was handled by a second-order explicit Newmark finite-difference scheme, with an additional Runge-Kutta scheme being used to march in time the memory variables needed to model viscoelasticity (see details in Komatitsch and Tromp, 1999).

Treatment of the Kinematic Source. To model the strong motion case S1, we considered a set of 1250 point sources regularly distributed on the prescribed fault plane. Each point source was assigned a moment magnitude M 2.9 and an onset time consistent with the imposed rupture kinematics.

Accuracy versus Efficiency. All simulations were performed on a cluster of 42 SUN-V40Z nodes equipped with four AMD-Opteron 2.6 GHz processors, each having 8 GB RAM. The computational parameters are summarized in Table 2.

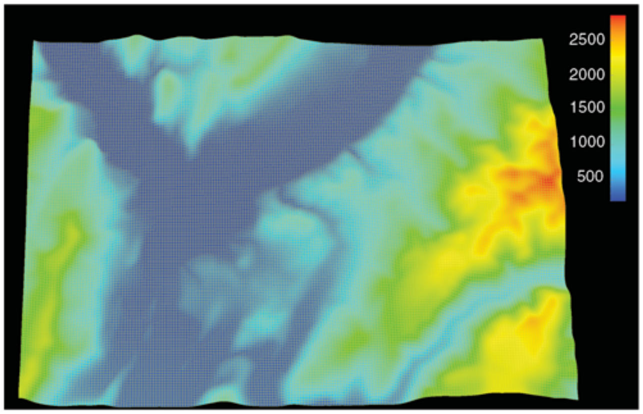

Figure 5. Surface view of the mesh of 192 × 160 elements used in the SEM1 calculations. The colors indicate surface elevation. The mesh contains 192 × 160 elements for 2 Hz calculations. The length of the elements does not vary horizontally and is kept smaller than 150 m. Each surface element contains 125 gridpoints (not shown here).

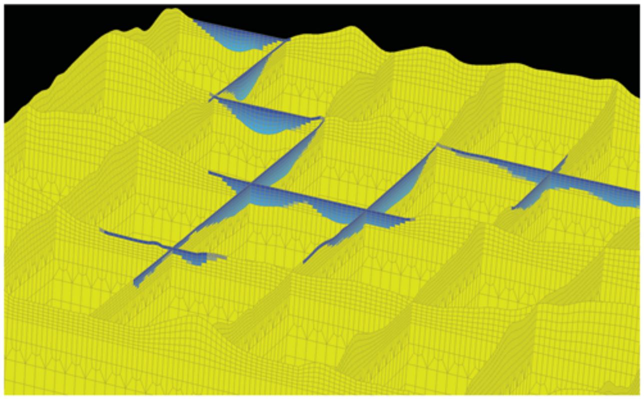

Figure 6. View of the 3D mesh of elements used in the SEM1 calculations. Golden colors indicate elements that are entirely within the bedrock, whereas blue colors stand for elements that intersect the sediments. The bedrock-sediment interface is not accounted for at depths shallower than 350 m, in particular for elements close to valley edges. The mesh is coarsened with depth following a simple conforming strategy proposed in (Komatitsch *et al.*, 2004).

3D Spectral-Element Method: The SEM2 Implementation

Model Geometry and Mesh Generation. In the second implementation of the SEM, SEM2, the meshing strategy adopted aims at accounting for true positions of material interfaces. This task was successfully solved thanks to the software CUBIT, which incorporates a set of powerful and advanced meshing schemes specifically developed to handle the hexahedral unstructured meshing problem (see the Data and Resources section for details). A thorough description of the meshing strategy adopted to strictly account for the geometry of the Grenoble Valley can be found in Stupazzini (2009). The final mesh is depicted in Figure 7 and consists of 216,972 elements, the size of which ranges from a minimum of about 20 m (inside the alluvial valley) up to 900 m. The mesh is designed to propagate frequencies up to 2 Hz with $N = 3$ (5,659,551 nodes) and up to around 3 Hz with $N = 4$ (13,300,892). A detailed zoom of a portion of the computational domain is presented in Figure 8, showing the strategy adopted to account for the discontinuity between the soft soil and bedrock. The computational domain is subdivided into small chunks; each of them is sequentially meshed starting from the alluvial basin down to the bedrock.

Material Heterogeneity and Attenuation. Inside the alluvial deposit the smooth vertical variation is taken into account assigning at each GLL point the mechanical properties evaluated according to the prescribed depth variation. The layer stratification is considered in the bedrock. The discontinuity between the soft soil and bedrock is strictly accounted for as previously mentioned. With respect to the constant quality factor model, frequencies smaller than 0.5 Hz will be overdamped, whereas higher frequencies will be enhanced in the alluvial deposits.

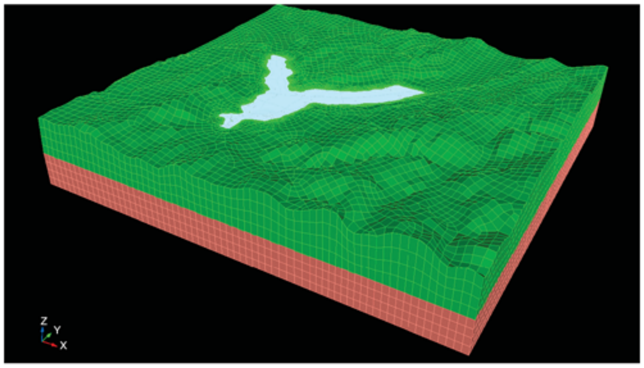

Figure 7. Three-dimensional view of the mesh used in the SEM2 calculations. The mesh contains 216,972 elements, ranging from 20 m (inside the alluvial basin) up to 900 m; for 2 Hz calculations $N = 3$ is sufficient. Different colors refer to different mechanical properties.

Treatment of the Kinematic Source. The seismic source is introduced through an appropriate distribution of the seismic moment tensor density (Aki and Richards, 2002). To model the strong motion case S1, we considered a set of 750 point sources regularly distributed on the prescribed fault plane.

Accuracy versus Efficiency. The simulations were performed on AMD Opteron 250 (64 bit single core 2.4 GHz) with 2 GB RAM and 1000T Ethernet (Oeser *et al.*, 2006). The computational parameters are summarized in Table 2.

3D Velocity-Stress Discontinuous Galerkin Scheme with ADER Time Integration of Unstructured Tetrahedral Meshes

Model Geometry and Mesh Generation. The ADER-DG method uses a tetrahedral mesh that accounts for the given geometry of the internal and external boundaries. Both the digital elevation model of the topography and the interface between the basin structure and the bedrock are provided on a regular grid with x-, y-, and z-coordinates, which is imported into a CAD tool to construct parameterized surfaces. These surfaces are then triangulated with an appropriate mesh size, and finally the volumes between the surfaces are filled with tetrahedral elements. Hereby the tetrahedral elements are conformingly connected to the surface triangulations. Furthermore, variable element sizes are chosen in order to account for the variable seismic velocity structure. Therefore, the edge lengths of the tetrahedral elements vary between 200 m inside the basin up to 5000 m at the bottom of the model, smoothly growing with increasing distance from the basin. Within the whole basin structure the mesh size increases vertically up to 500 m at the bottom of the basin.

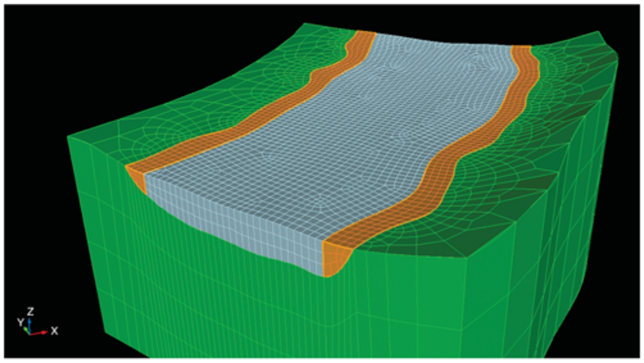

Figure 8. In order to account for the discontinuity between soft soil and bedrock the computational domain is subdivided into small chunks, each of them is sequentially meshed starting from the alluvial basin down to the bedrock.

In order to capture the topography sufficiently accurately the lateral growths factor along the free surface is chosen to result in a maximum edge length of 1000 m at the top lateral boundaries.

Material Heterogeneity and Attenuation. The smooth vertical heterogeneities inside the basin and in the surrounding bedrock are approximated in the ADER-DG approach by piecewise constant material; that is, the material parameters are evaluated at the barycenter of a tetrahedral element and are then assumed to be constant within the volume covered by the element. Similarly, the Q-factor for the viscoelastic material properties inside the basin is evaluated at the barycenter. The given wave velocities at that position are then assumed to be given for a central frequency of 1 Hz within the absorption band from 0.1 to 10 Hz. The frequency-independent constant Q-law is approximated with three relaxation mechanisms defined by a generalized Maxwell body.

Treatment of the Kinematic Source. The ADER-DG method treats the source term in both cases (W1 and S1) as a kinematic seismic source. Whereas the W1 case uses a single, double-couple point source with given location and source parameters, the S1 source is represented by 5000 aligned slip patches of a dimension of 90 m × 90 m to cover the specified 9 km × 4.5 km fault surface. Each slip patch is treated as a point source with the same parameters (strike, dip, rake) and the same shape of the source time function and possess different onset times as derived from the given rupture velocity. Therefore, the resulting seismic wave field is generated as a superposition of all individual slip patches.

Accuracy versus Efficiency. The simulations were performed on Intel Itanium2 Madison processors 1.6 GHz, 4 GB RAM per node. The computational parameters are summarized in Table 2.

Comparison of Numerical Predictions

Outline of the Comparison Method

Comparing numerical predictions of ground motion in a realistic 3D application is not straightforward because no reference solution is available, and each prediction may come with its own errors, either intrinsic (due to the limitations of the numerical method used) or case-dependent (due to implementation and human errors). While it can be assumed that intrinsic errors can be identified by a proper knowledge of the numerical method being used, implementation errors need more user experience and often a complex iterative process to be tracked and hopefully minimized.

Here we present the results of such comparison process for the Grenoble Valley between four implementations of the numerical techniques presented before: DGM based on the discontinuous Galerkin method, FDM based on the finite-difference method, and SEM1 and SEM2, two implementations of the spectral-element method. We carefully checked that the presented numerical predictions are not affected by technical mistakes in individual implementations and simulations.

We compare the ground-motion predictions for the weak and strong motion cases W1-FLAT and S1-FLAT, respectively. The comparison includes a visual inspection of ground acceleration at selected receivers and global maps of peak ground velocity, as well as a quantitative analysis based on two different measures introduced recently: the goodness-of-fit score proposed by Anderson (2004), which consists of an average of ground-motion indicators of common use in engineering seismology, and the misfit measure proposed by Kristekova *et al.* (2006), which is based on the time-frequency representation of the seismograms.

Finally, we present the results obtained for the strong motion case S1-TOPO and compare the different predictions of the effects of surface topography.

Peak Velocities

Figure 9 shows the global maps of PGV (i.e., the peak values of the norm of the ground velocity vector) computed for the strong case motion case S1-FLAT by the four codes: DGM, FDM, SEM1, and SEM2.

Note the high level of ground motion for this M 6 event, especially in the eastern part of the valley. Lower values would be obtained by choosing a more physical source kinematics (instead of the Haskell model considered here, which produces a very strong directivity effect on the S wave) and depth (the top of the fault for the S1 event is located only 750 m below sea level, or about 1.5 km below surface). All maps show little correlation with the sediment thickness, except near the receiver R21, where the low values of ground velocity are consistent with the presence of steep bedrock uplift (see Fig. 2). The strongest amplitudes occur in the southeast part of the valley, with peak velocities exceeding 1.5 m/sec. These localized high values are caused by late interferences of surface waves diffracted off the eastern edge of the valley with surface waves backscattered off the bedrock uplift.

The PGV maps computed by the four codes look remarkably similar. Subtle differences can be seen, for example, in the source region where the patterns differ slightly. This could indicate small differences in the implementations of the extended source. Also, the level of the peak values displayed by the FDM code seems systematically larger than that of the other predictions. However, given the intrinsic difficulty of comparing peak values, the level of agreement shown in Figure 9 is found to be satisfactory.

Quantitative Comparison

Similarity Score and Misfit Measure. The issue of assessing the reliability of numerical predictions of ground motion has received renewed interest in recent years with the introduction of new tools to quantify the fit, either between synthetics and observations or between numerical predictions.

Anderson (2004) proposed a measure of the goodness-of-fit between two seismograms that is based on the comparison of 10 criteria that are commonly used in engineering applications: Arias duration (criterion1, or C1), energy duration (C2), Arias integral (C3), energy integral (C4), peak acceleration (C5), peak velocity (C6), peak displacement (C7), response spectrum (C8), Fourier spectrum (C9), and cross correlation (C10). These criteria are evaluated in narrow frequency bands and scaled between 0 and 10. A global average (between individual criteria and different frequency bands) is then applied to end up with one number, the so-called similarity score. Based on the systematic comparison of the horizontal components of recorded motions, Anderson (2004) introduced the following verbal scale for goodness-of-fit: a score below 4 is a poor fit, between 4 and 6 is a fair fit, between 6 and 8 is a good fit, and beyond 8 is an excellent fit.

Figure 10 shows an example of calculation of the similarity between the predictions of the north–south ground acceleration at the borehole receiver R06 for the S1-FLAT case. Solution SEM1-FLAT is used as a reference for all measurements, and only one frequency band, 0.1,2 Hz, is considered. Figure 10 confirms the impression of good fit from visual inspection of seismograms. It also shows that the differences between predictions obtained by different codes are smaller than the difference between predictions obtained by the same code with and without including the effect of surface topography (SEM1-FLAT and SEM1-TOPO).

Kristekova *et al.* (2006) proposed a measure of the misfit between two seismograms, which relies on the time-frequency representations of the signals. Their time-frequency misfit measure (hereafter referred to as TF misfit measure or simply TF misfit) allows separating amplitude (envelope) and phase differences both in the time and frequency domains.

Figure 11 shows an example of application of the TF misfit to the predictions of north–south ground acceleration at R06 for the S1-FLAT case by the FDM and SEM1 codes. The figure shows the time-frequency envelope (amplitude) and phase misfits, respectively, denoted by TFEM and TFPM. An average of the absolute values of TFEM and TFPM over time and frequency results in single-valued estimations of the envelope (EM) and of the phase (PM) misfits. A single,

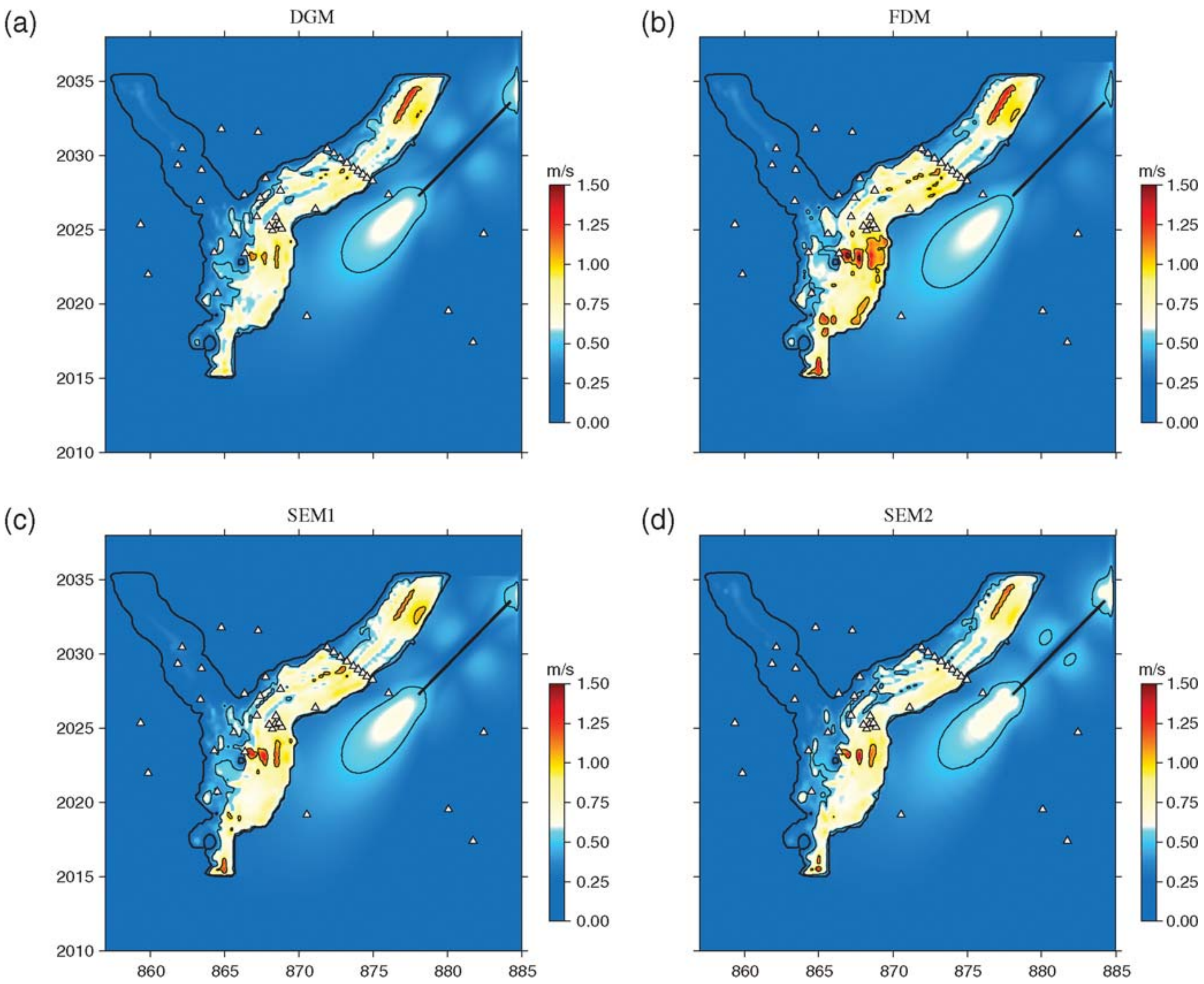

Figure 9. PGV maps obtained by the four codes (a) DGM, (b) FDM, (c) SEM1, (d) SEM2 for the strong motion case S1 without surface topography (S1-FLAT). Receiver locations are indicated by the triangles. The X and Y labels denote distances (in km) in the local Lambert coordinate system. The bold curve indicates the 50 m contour line in the sediment thickness map and the bold straight line shows the surface projection of the fault for the S1 event.

global score (denoted by EPM) is finally obtained by averaging EM and PM.

Application to the S1-FLAT and W1-FLAT Cases. We computed both the similarity score and the TF misfit for all 40 receivers and all predictions, taking the SEM1 result as a reference. We chose to use a single reference to alleviate the task of computing the misfits for each pair of predictions. Our analysis was performed for a time window 0,20.48 sec (2048 samples with timestep $\Delta t = 0.01$ sec) for each component of ground acceleration.

The correspondence between the similarity score and the TF misfit is summarized in Figure 12. Each dot represents a pair of measures evaluated at a single receiver, on a single component of ground acceleration for one of the cases S1-FLAT, S1-TOPO, or W1-FLAT. The figure shows a linear trend between the results of the two measures, which is particularly accurate for well-matching predictions. The level of the excellent fit, defined by Anderson (2004) as the similarity score above 8, corresponds to a TF misfit level below 0.4. The equation of the linear regression writes $(10\text{-}S) = 5M$, where S and M stand for the similarity score and TF misfit, respectively. Based on this equivalence, we will hereafter represent the results of the comparison of numerical predictions using the sole TF misfit measure.

We found no significant dependence of the TF misfit on the ground-motion component considered: the mean difference (averaged over the 40 receivers) between different single-component TF misfits does not exceed 0.04 (or 0.2 in terms of the similarity scores). We will therefore use a unique misfit value at each receiver, referred to as the total misfit, and defined as the arithmetic mean of the three individual TF misfits computed for the X, Y, and Z components.

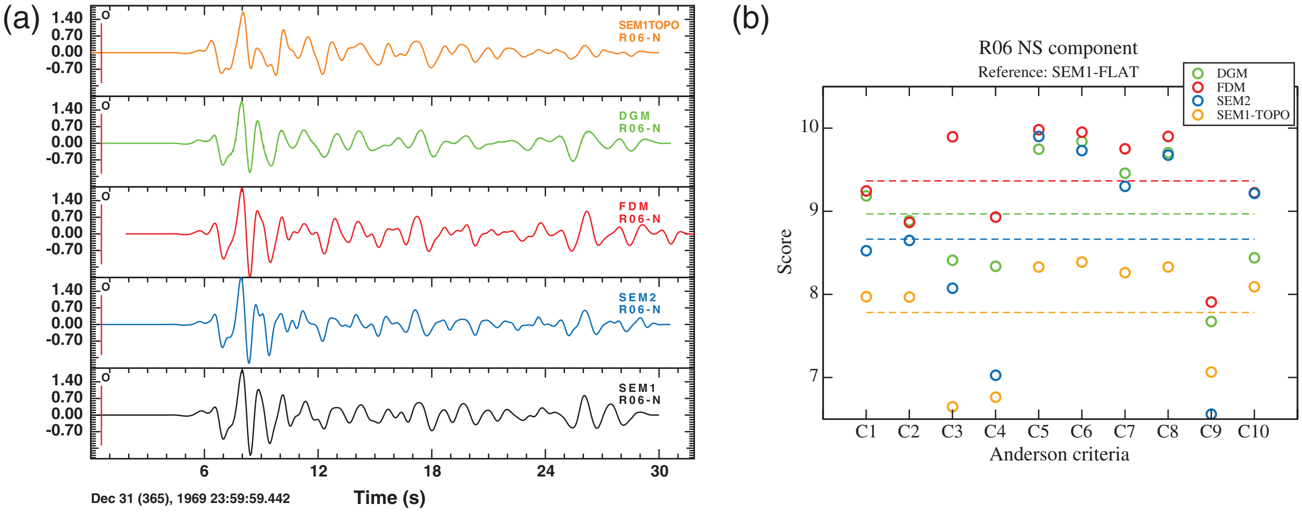

Figure 10. (a) Time series of the NS ground acceleration computed at receiver R06 by 4 different codes for the strong motion case S1-FLAT: DGM (green), FDM (red), SEM1 (black), and SEM2 (blue). The topmost trace (orange curve) was computed by the code SEM1 including surface topography (S1-TOPO). (b) Goodness-of-fit as measured by the 10 criteria proposed by Anderson (2004). The SEM1-FLAT prediction is used as reference in each case. The dashed lines indicate the levels of the global similarity scores for each prediction. Note that the fit between different predictions of the same simulation case (S1-FLAT) is better than the fit between predictions of different simulation cases (S1-TOPO and S1-FLAT) by the same code (SEM1).

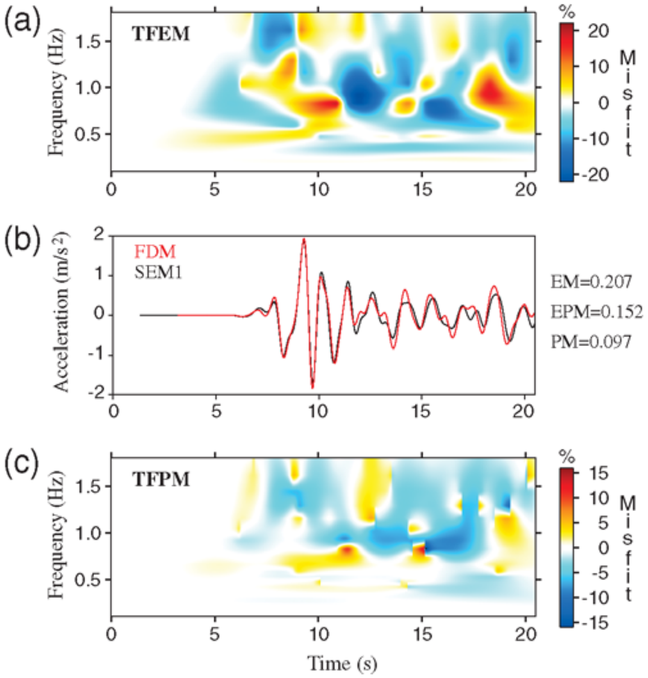

Figure 11. Example of application of the TF misfit analysis to the predictions of the NS ground acceleration at receiver R06 for the S1-FLAT case. (a),(c) Panels show the time-frequency envelope (TFEM) and phase (TFPM) misfits, respectively, taking the SEM1 prediction as a reference. (b) Time series of acceleration predicted by codes FDM (red) and SEM1 (black) are shown. Single-valued envelope (EM) and phase (PM) misfits are obtained by averaging the absolute values of TFEM and TFPM over time and frequency. The total TF misfit is obtained by averaging the envelope and phase misfits EM and PM.

Figure 13 shows the TF misfits between the different predictions of the S1-FLAT and W1-FLAT cases computed at the 40 receivers in the frequency band 0.1–2 Hz. Each dot corresponds to the total TF misfit averaged over the three components of ground acceleration.

For the S1-FLAT case, the misfit between the different predictions is almost everywhere lower than 0.4, which corresponds to the level of the excellent fit defined by Anderson (2004). Note the high similarity between the predictions of the FDM and SEM1 codes, despite the systematic amplitude shift observed in Figure 9. This illustrates the importance of

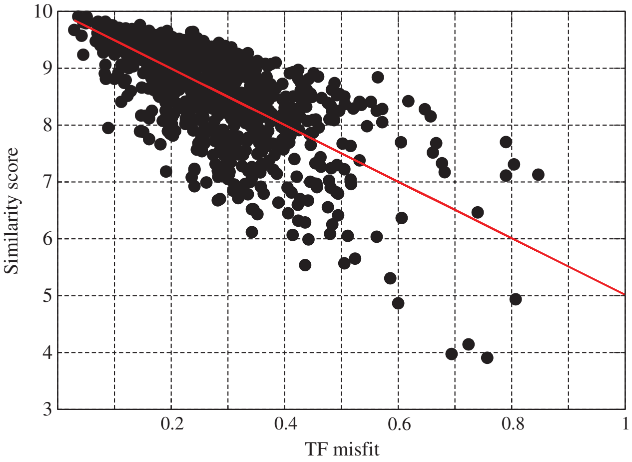

Figure 12. Comparison of results obtained with the TF misfit (M) plotted against those using the similarity score (S). Both measures have been applied to the 3 components of the 40 receivers for the benchmark cases S1-FLAT, S1-TOPO, and W1-FLAT. A global linear trend (red line) with equation ($10\text{-}S = 5M$) is found.

using a quantitative misfit measure instead of a single ground-motion parameter. Although the implementation of the point source is expected to be much simpler, the level of misfit is higher for the weak-motion case W1-FLAT than for the strong-motion case S1-FLAT. This is related to the larger high-frequency content of the W1 source, compared with the S1 source, which challenges the numerical methods at hand. Individual time series and amplitude spectra of the three components of ground acceleration at receiver R02, located in the center of the Grenoble Valley, are shown in Figure 14 and Figure 15 for the S1-FLAT case and W1-FLAT case, respectively.

Visual inspection of the traces and spectra confirms the high similarity between the different predictions of the S1-FLAT case, including at late arrival times, whereas larger differences in amplitude and phase arise for the predictions of the W1-FLAT case. Note in particular in Figure 15 the differences in timing and amplitude between the predictions of the diffracted Rayleigh wave arriving around 8 sec. Because of the wider frequency content of the source, the weak motion case also tends to highlight the differences in the implementation of intrinsic attenuation as described in the previous section (see, for example, the larger high-frequency content of the SEM2 prediction compared with the others).

Figure 16 and Figure 17 show the results obtained for the S1-FLAT case at two other locations: R06 (Montbonnot borehole ground-level station) in the middle of the 2D profile across the Grésivaudan Valley and R21 close to the steep bedrock uplift (see Fig. 2). Note the high similarity between all predictions at receiver R06 and the differences in amplitude and phase that lead to the large misfit between SEM1 and DGM at R21. This last example (R21) is one of the only cases where the level of misfit is surprisingly high in one component only (Z).

The global TF misfit distributions displayed in Figure 13 do not show any particular dependence on either the soil condition or the receiver location within the valley. The main trend is a systematic increase of the misfit with increasing distance to the source. This is expected because intrinsic errors (e.g., numerical dispersion) or differences in physical modeling (e.g., intrinsic attenuation) tend to accumulate with time and with the distance propagated. In the remainder of this section, we will therefore represent the misfit as a function of the source-receiver distance. The detail of the TF misfits in terms of amplitude and phase is shown for the S1-FLAT case in Figure 18. Both measures show the same pattern, with the highest similarity being found between the FDM and SEM1 predictions. However, the phase misfit seems to be more helpful in tracking differences between predictions. For example, the amplitude misfit between DGM and SEM1 is roughly identical to the one between SEM1 and SEM2, but larger phase misfits are seen between SEM1 and SEM2. Note also that the increase of the total TF misfit between FDM and SEM1 predictions with distance only appears in the amplitude (envelope) misfit, the difference in phase being roughly constant for all 40 receivers.

To better understand the differences between numerical predictions for the S1-FLAT case, we plot in Figure 19 the amplitude and phase misfits computed in three frequency bands: low-frequency (LF) 0.2,0.5 Hz; intermediate frequency (IF) 0.5,1.0 Hz; and high-frequency (HF) 1.0,2.0 Hz. Note that the LF band is roughly centered at the fundamental frequency of the Grenoble Valley (around 0.3 Hz); the energy radiated by the source in the S1-FLAT case decreases significantly in the HF band, suggesting that the weight of the HF misfit in the total TF misfit is weak. There is a global trend for the TF misfits (amplitude and phase) to increase with frequency. Therefore, it becomes more difficult at higher frequencies to assume a linear dependence on the source-receiver distance. This can be mainly explained by the fact that intrinsic errors of each numerical method (in particular numerical dispersion) increase with frequency.

We finally remark that there is a strong dependence of the amplitude misfit between DGM and SEM1 with frequency, which results in large differences in the HF band. The TF misfits computed for the W1-FLAT case (see Fig. 13) suggest that these discrepancies become dominant when the high-frequency content of the source is larger.

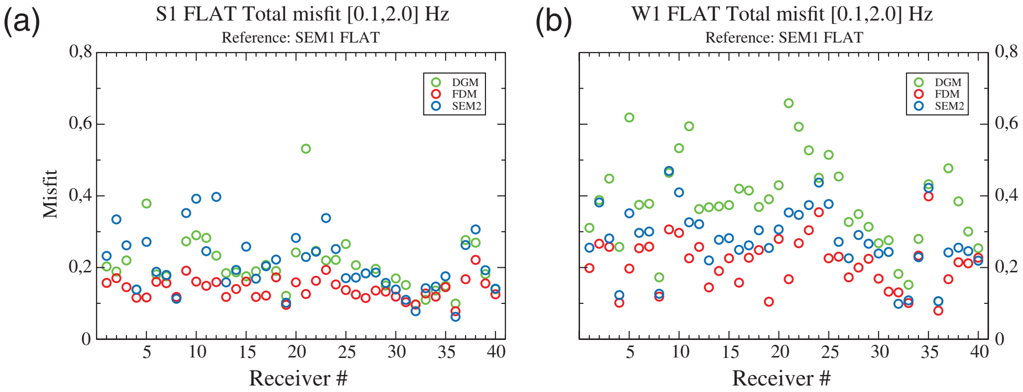

Figure 13. (a) TF misfits computed for the S1-FLAT case and (b) for the W1-FLAT case, taking the SEM1 prediction as reference. Each dot corresponds to the average of the 3 components of total misfit (average of envelope and phase) measured on the predictions of ground acceleration at each receiver in the frequency band 0.1,2.0 Hz. Receivers R01, R04, R08, and R33–R40 are located on rock sites.

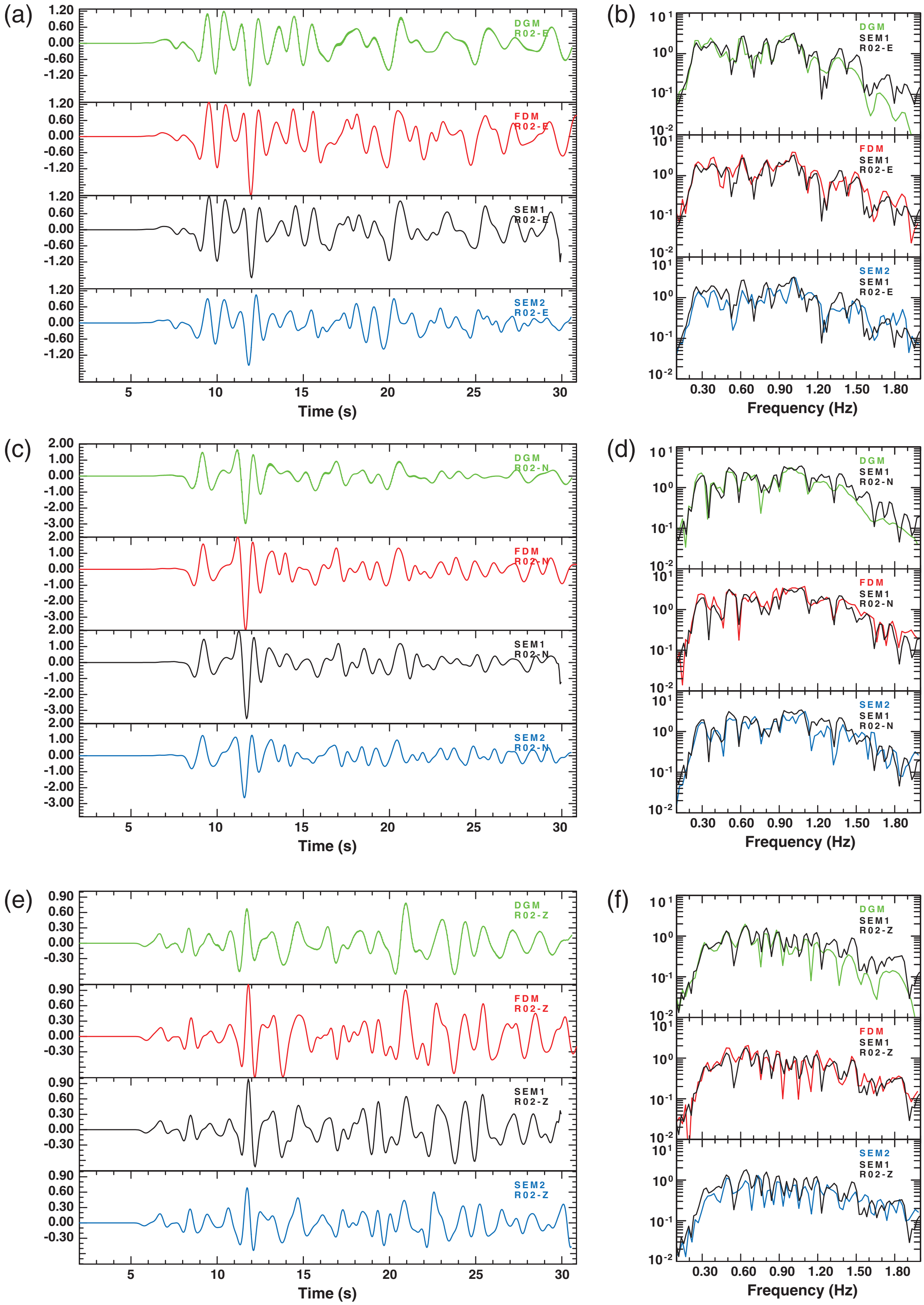

Figure 14. (a),(c),(e) Time series and (b),(d),(f) amplitude spectra of ground acceleration (EW, NS, UD) computed at receiver R02 by the four different codes for the strong motion case S1-FLAT.

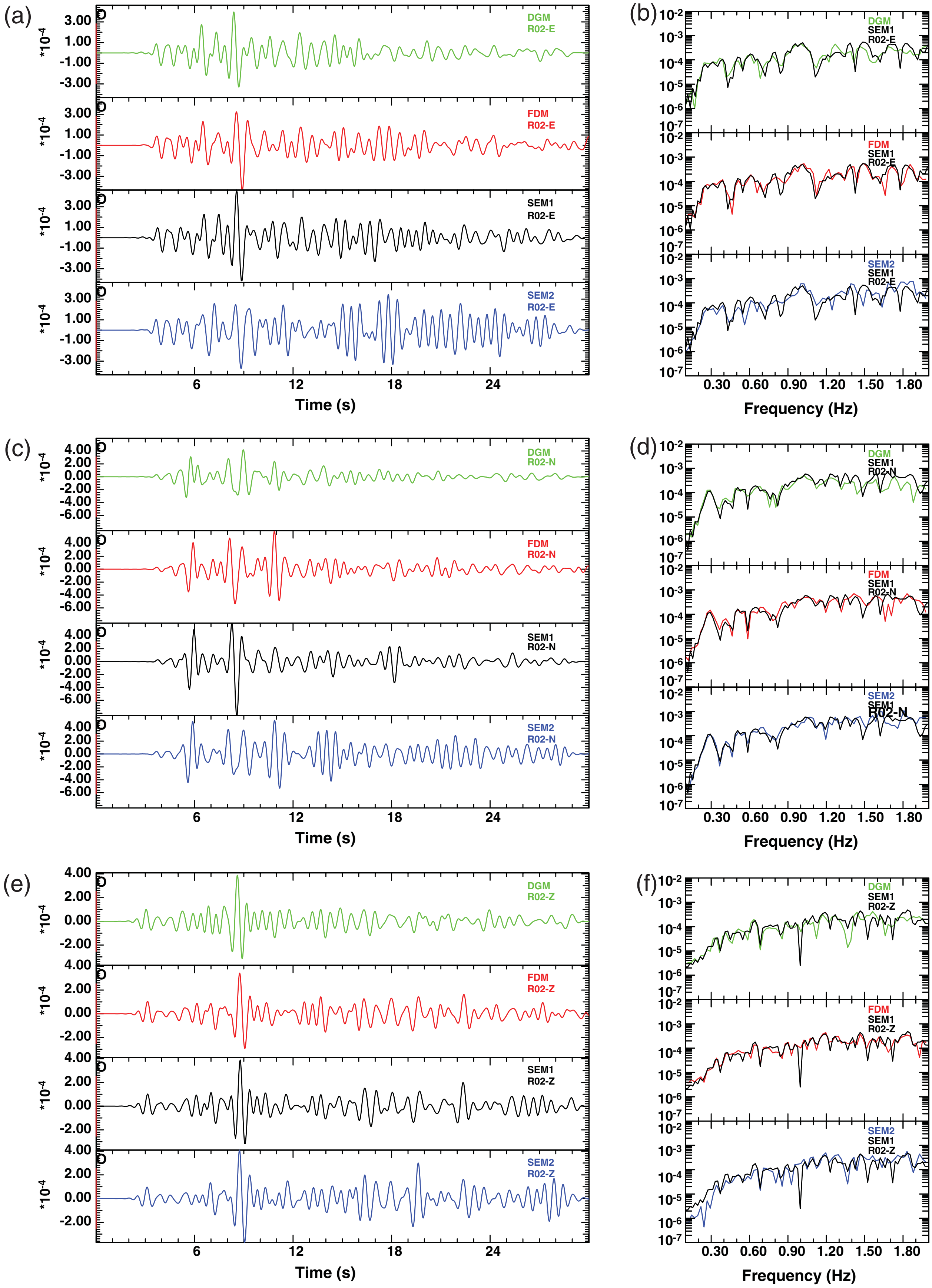

Figure 15. Same as Figure 14 for the weak motion case W1-FLAT.

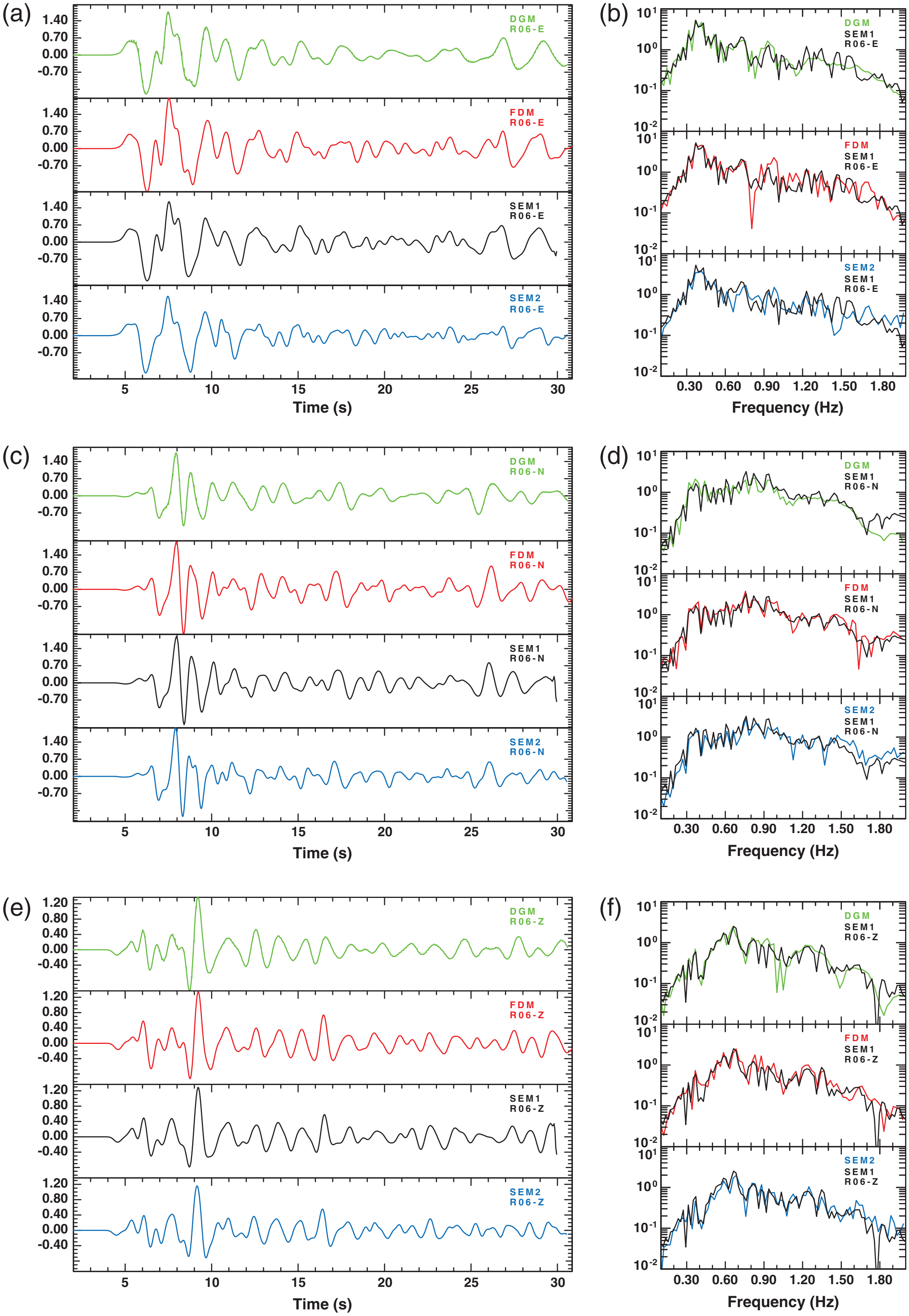

Figure 16. (a),(c),(e) Time series and (b),(d),(f) amplitude spectra of ground acceleration (EW, NS, UD) computed at receiver R06 by the four different codes (DGM, FDM, SEM1, and SEM2) for the strong motion case S1-FLAT.

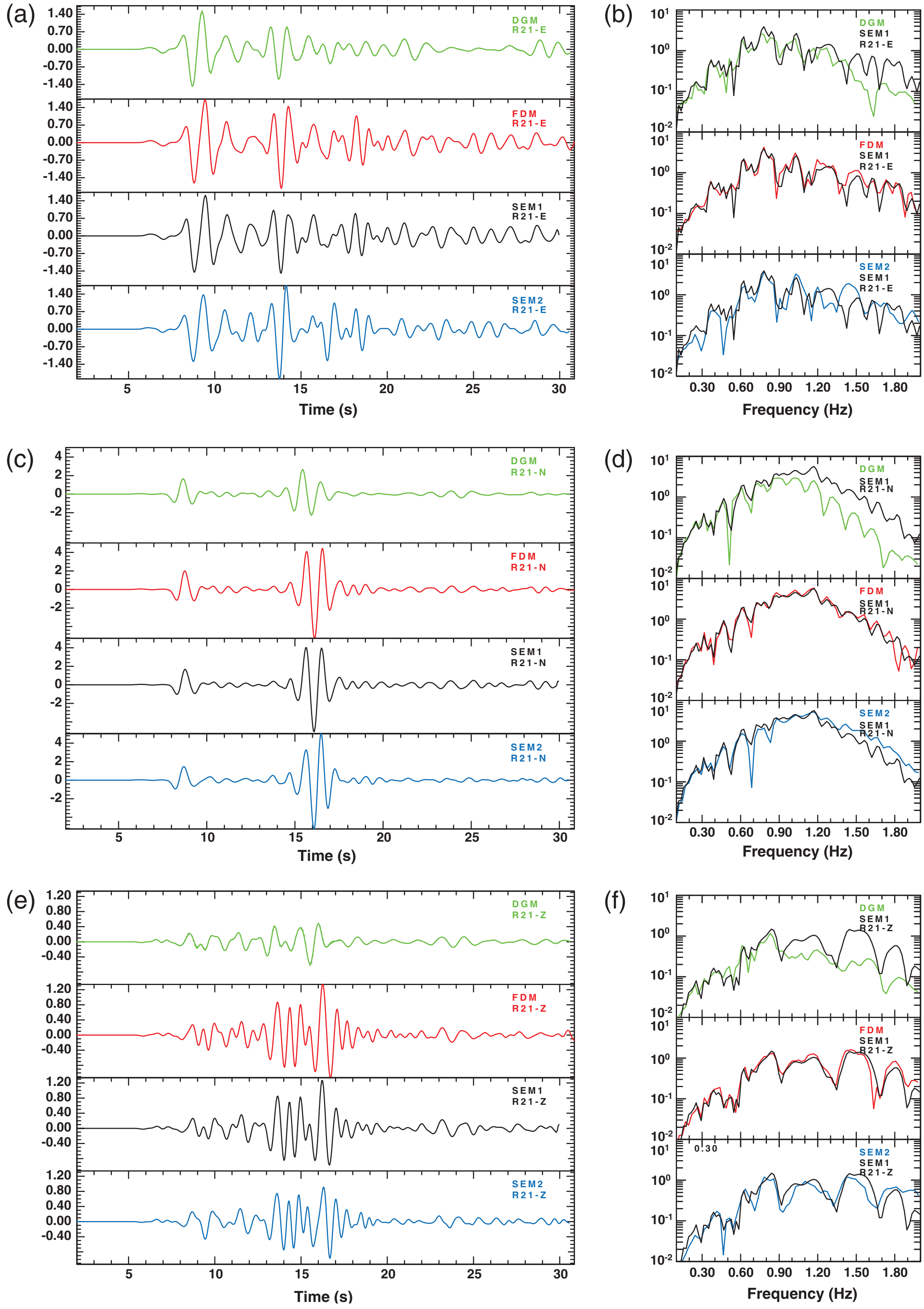

Figure 17. (a),(c),(e) Time series and (b),(d),(f) amplitude spectra of ground acceleration (EW, NS, UD) computed at receiver R21 by the four different codes for the strong motion case S1-FLAT. Note the low similarity between the DGM and SEM1 predictions on the vertical component.

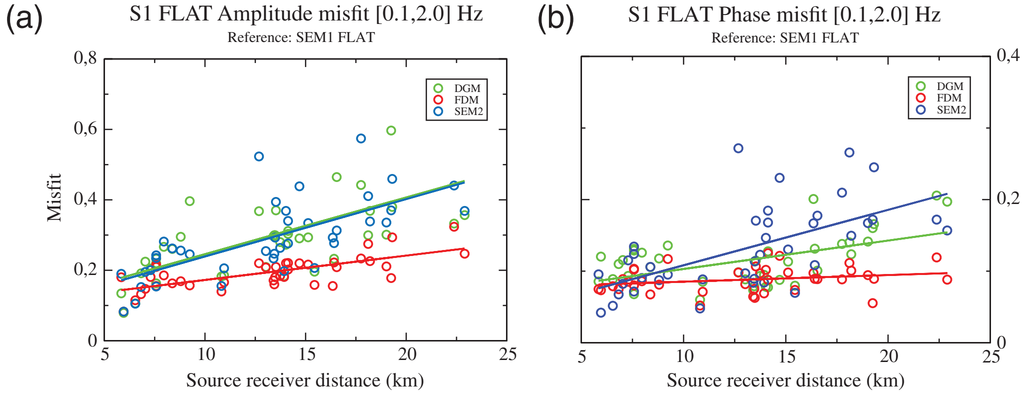

Figure 18. (a) Envelope and (b) phase misfits computed for the S1-FLAT case and plotted against source-receiver distance. Solid lines indicate linear regressions through the sets of points.

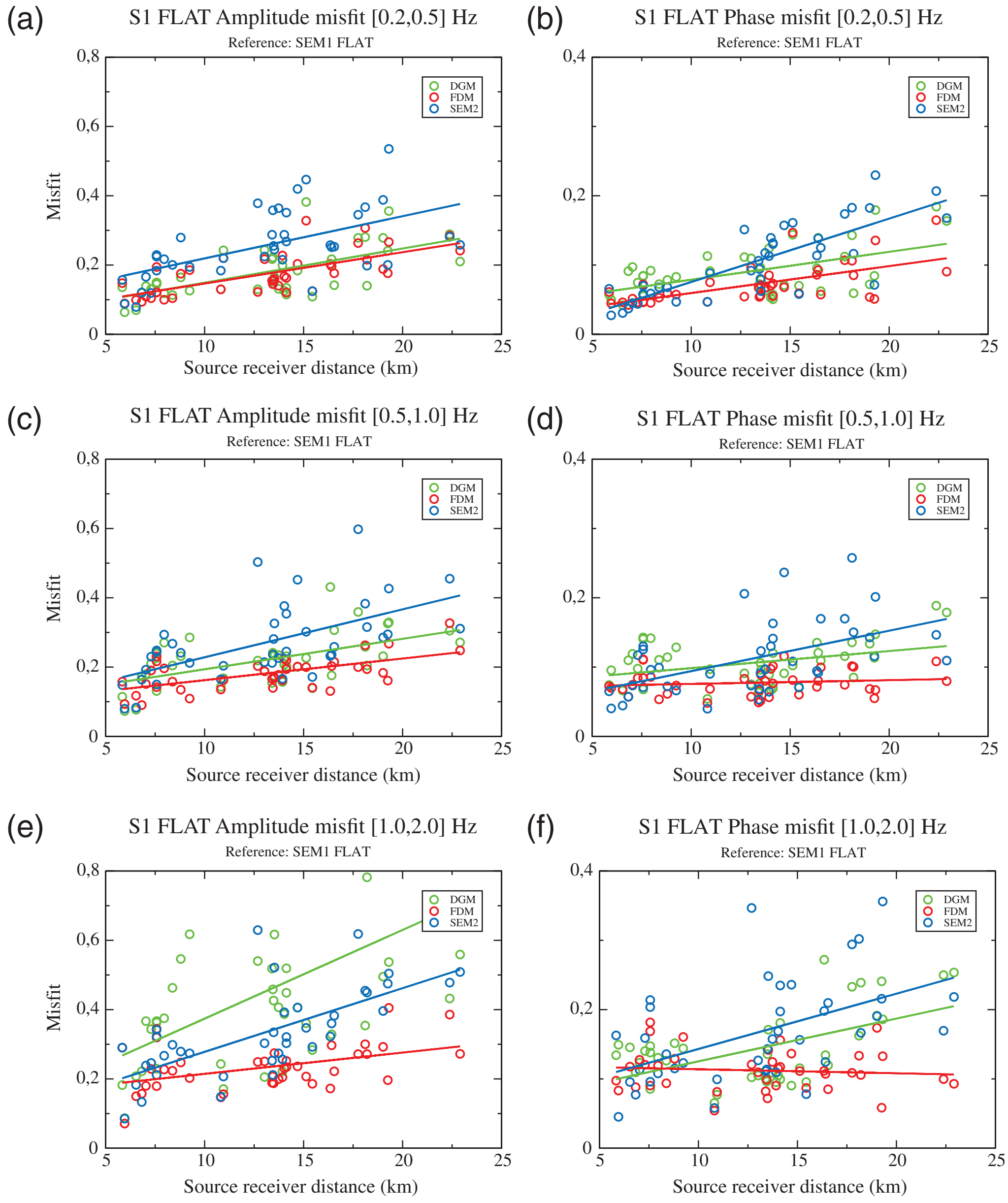

Figure 19. Same as Figure 18 for different frequency bands: (a),(b) 0.2,0.5 Hz; (c),(d) 0.5,1.0 Hz; and (e),(f) 1.0,2.0 Hz.

Effect of Surface Topography

Three codes (DGM, SEM1, and SEM2) computed the strong motion case S1-TOPO, which includes the effect of surface topography. The PGV maps obtained for the S1-TOPO case are shown in Figure 20. Note the deformation of the predicted patterns (compare with Fig. 9) close to the source due to the presence of surface topography on top of the fault plane. The overall distributions of peak values look quite similar inside the valley, suggesting that the main differences with respect to the S1-FLAT case occur on the rock sites. This is only partly confirmed by Figure 21, which shows the maps obtained by dividing the PGV by those obtained in the S1-FLAT case. Noticeable differences are indeed observed in the southwestern part of the valley, a region where strong variations of the sediment thickness occur. The patterns observed on the three maps of PGV ratios are quite consistent outside of the valley: systematic amplification is found on the mountain peaks (see, for example, receivers R33 and R34 in the eastern Belledonne chain and receivers R39 and R40 in the northern Chartreuse massif), whereas deamplification is found in valleys (see receiver R35). Seismic motion on slopes is more complex because amplification or deamplification can occur depending on the slope orientation with respect to the seismic event (see the two flanks bordering the Romanche Valley around receiver R35 at coordinates $X = 880$ km, $Y = 2015$ km). Extreme and mean values of amplification and deamplification are given in Table 3.

The average effect of surface topography inside the valley, as measured by the ratio of the PGV, is found to be negligible, but large differences in extreme values occur: the maximal predicted amplifications vary significantly on

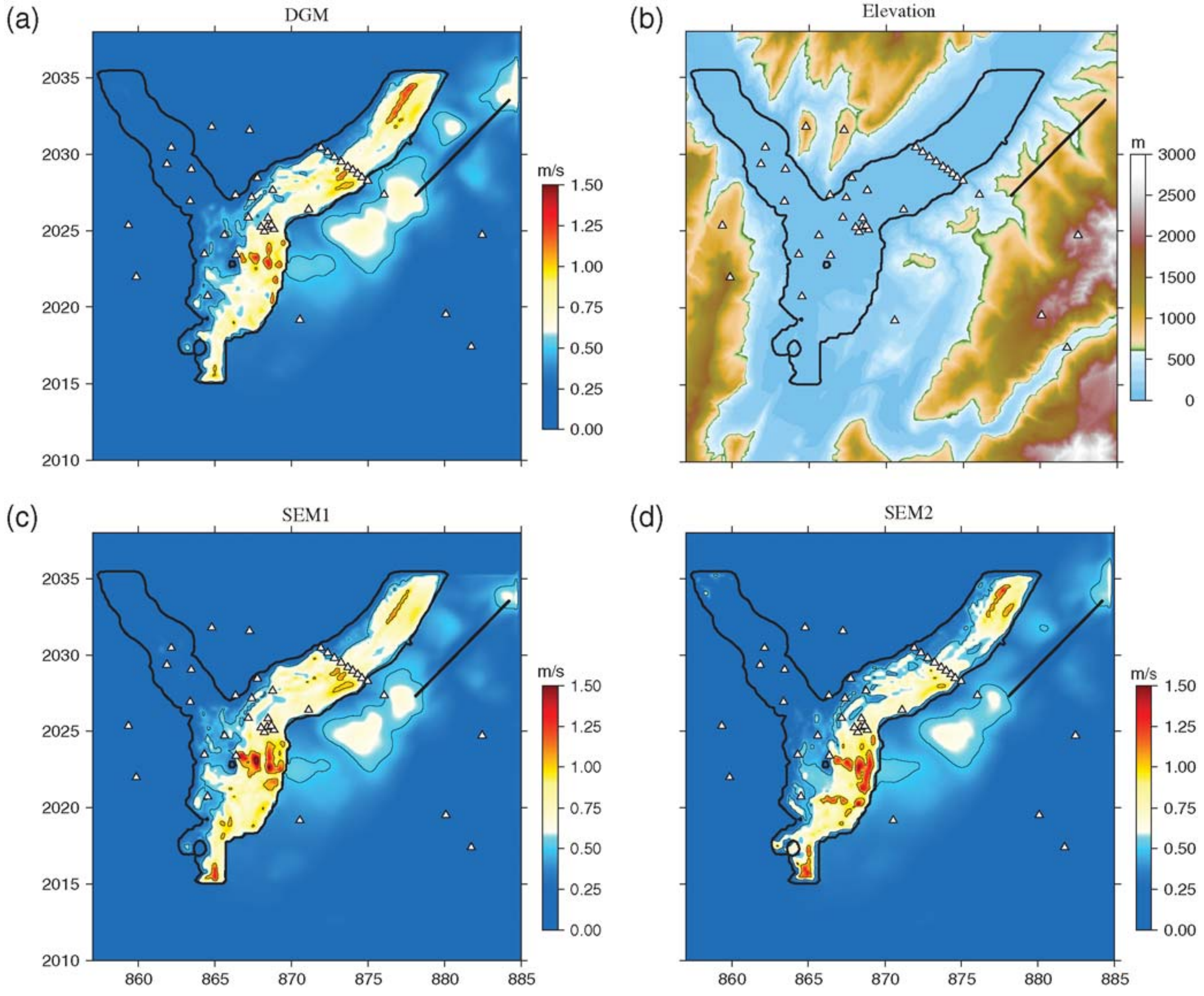

Figure 20. PGV maps obtained by three codes: (a) DGM, (c) SEM1, (d) SEM2 for the strong motion case S1-TOPO. (b) The map of surface elevation is shown. Receiver locations are indicated by the triangles; the X and Y labels denote distances (in km) in the local Lambert coordinate system. The bold curve indicates the 50 m contour line in the sediment thickness map; the bold straight line shows the surface projection of the fault for the S1 event.

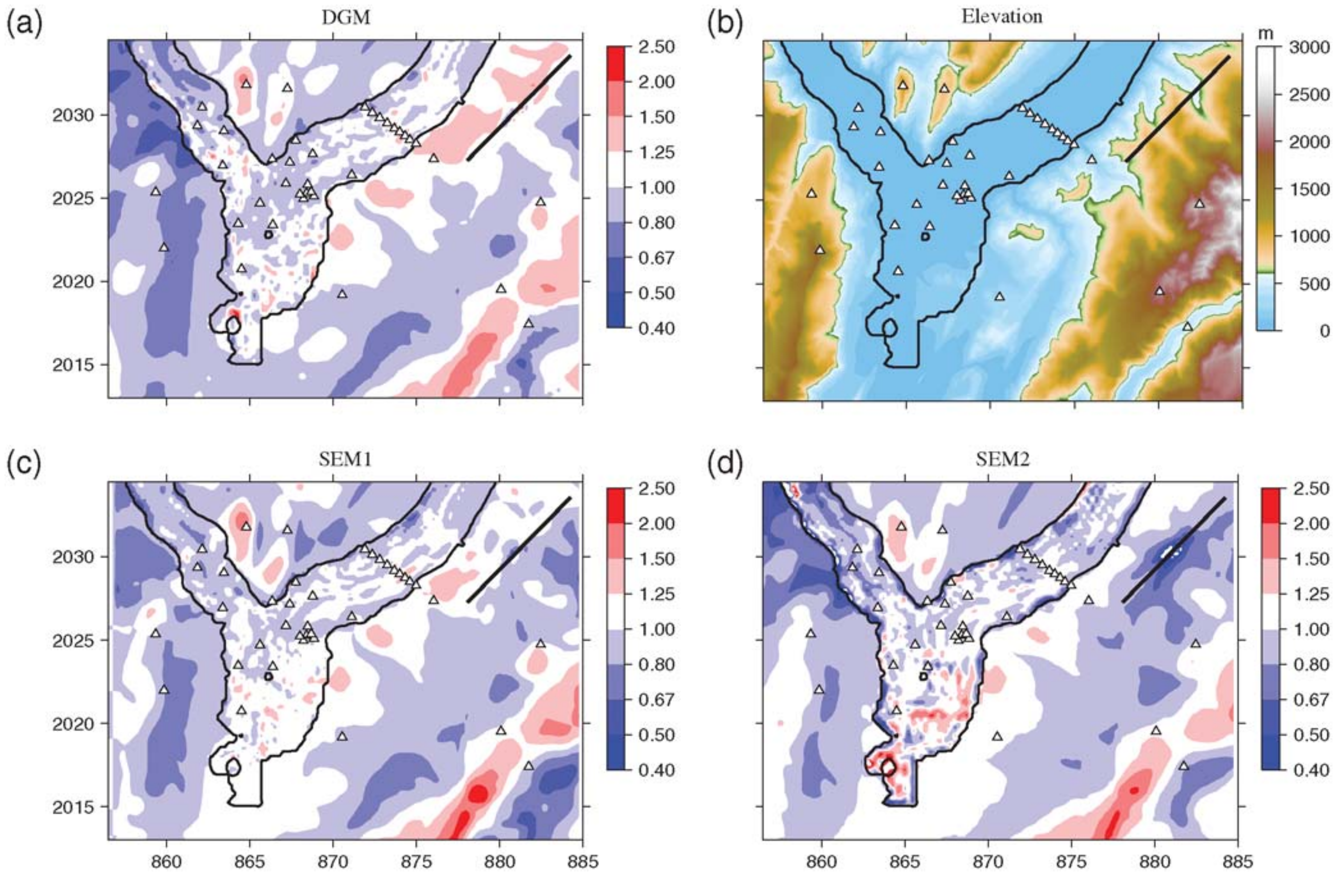

Figure 21. Maps of ratios between the PGV obtained with the surface topography and PGV obtained for the flat free surface by the three codes: (a) DGM, (c) SEM1, and (d) SEM2. (b) The map of surface elevation is shown. Receiver locations are indicated by the triangles and the *X* and *Y* labels denote distances (in km) in the local Lambert coordinate system. The bold curve indicates the 50 m contour line in the sediment thickness map and the bold straight line shows the surface projection of the fault for the S1 event.

rock sites and, more surprisingly, within the valley. This could result from differences in the implementation of surface topography, in the representation of velocity contrasts near the valley edges, and in the design of the meshes for the S1-FLAT and S1-TOPO cases.

Conclusions

The third international symposium on the effects of surface geology in Grenoble, France (ESG 2006), provided an excellent opportunity to focus the traditional blind prediction experiment on numerical modeling of earthquake motion in a typical deep Alpine sediment-filled structure, the Grenoble Valley.

The Grenoble urban area gathers a significant population of around 500,000, a number of high-tech and sensitive industrial facilities, and educational and research institutions. This and observed broadband site effects imply that the moderate regional seismic activity poses a concern about the seismic risk in the area. Moreover, similar conditions are also met in other areas within the European Alps and in other mountainous areas with embanked valleys filled with young, postglacial lacustrine sediments. This specific area also presents a further interest in relation to its relatively small extent, which allows performing deterministic numerical simulation up to higher frequencies than is usually considered in much wider areas such as the Los Angeles basin.

The present article reports partial results from this simulation exercise for four structure wave-field configurations that were specified for voluntary participants: W1-FLAT, S1-FLAT, W1-TOPO, S1-TOPO, with *W* and *S* meaning weak and strong, FLAT and TOPO meaning geometry of the free surface, respectively. The weak configurations comprised

Table 3

Extreme and Average Values of the Ratio of Peak Ground Velocity Computed by the Codes DGM, SEM1, and SEM2*

	DGM	SEM1	SEM2
Minimum ratio (valley)	0.447	0.549	0.133
Maximum ratio (valley)	2.255	1.641	3.599
Mean ratio (valley)	0.996	0.998	0.991
Minimum ratio (rock)	0.543	0.533	0.277
Maximum ratio (rock)	3.222	2.464	2.095

*With and without accounting for the effects of surface topography.

double-couple point sources, the strong ones finite kinematic source models.

Fourteen groups from eight countries contributed to the ESG 2006 comparison with at least one numerical method and possibly different cases, providing a total of 18 prediction sets; seven groups addressed the 3D problem, out of which three could account for the effects of both underground and surface topography. The numerical schemes used for the 3D contributions belong to the finite-difference, spectral-element, and discontinuous-Galerkin finite-element methods. Four participants whose 3D predictions were surprisingly close updated their results after the ESG meeting, after correcting some nonmethodological errors (evidenced by comparing to other predictions) in preparation of the numerical simulations. Only the results from the corrected predictions were considered here.

One of the main lessons of this comparative exercise concerns the present capabilities of numerical simulation and is indeed a lesson of modesty: all the submitted predictions exhibit a very large variability. This variability confirms that the numerical prediction of ground motion in general certainly cannot be considered a mature, push-button approach, and the variability in direct uncorrected numerical predictions can be significantly larger than the variability associated with empirical predictions. This is also because not all applied numerical codes implement the best methodologically possible algorithms; some of the codes are not yet bug free. Much care should be also given to an unambiguous definition of the input solicitation (input signal and/or source kinematics). Not sufficiently elaborated numerical predictions may yield wrong results and therefore will lead to large mistrust from end users.

However, there is also another lesson, which is a lesson of hope: the striking similarity between predictions by completely different numerical methods is a very encouraging result. Despite the structural complexity, that is geometry and relatively large velocity contrast at the sediment-basement interface as well as smooth heterogeneity, and the methodological differences among the simulation methods, we found a surprisingly good level of agreement among four of the submitted predictions obtained by the finite-difference method (FDM), two implementations of the spectral-element method (SEM1 and SEM2), and arbitrary high-order derivative, the discontinuous Galerkin method (ADER-DGM). It clearly shows that, when used with caution, numerical simulation is actually able to handle wave radiation correctly from an extended source and their subsequent propagation in complex 3D media.

The expression good agreement is not simply a matter of subjective feeling. It indeed results from a detailed, quantitative comparison between the four numerical predictions using the misfit criteria proposed by Kristekova *et al.* (2006). These misfit criteria are based on the time-frequency representations of the signals and allow proper quantification and characterization of disagreement between signals. This misfit measurement is found to be consistent with the engineering-oriented similarity score proposed by Anderson (2004). Another instructive comparison was achieved by looking at predicted PGV maps.

The main conclusions from the detailed comparison are explained in the following list:

- The objective quantification of the mismatch between the different predictions proves to be effective and useful. The two different comparison tools used for quantification, although very different, do provide very consistent results. While Anderson's engineering-based criteria are probably enough for validating numerical predictions for end users, more refined comparisons based on time-frequency analysis greatly help in understanding the origin of differences. In particular, the analysis of the phase misfit with the technique of Kristekova *et al.* (2006) proves very instructive in identifying differences in propagation properties from one numerical method to another, and thus in orienting further investigations to refine computational tools.
- The match is found to be good at low frequencies (below 1 Hz) and to gradually deteriorate with increasing frequency, as expected. The reasons for that could not be unambiguously individualized, but may be related both to differences in the numerical methods (numerical dispersion, implementation of damping) and differences in the model implementation.
- An important component to explain the differences is certainly related to the meshing. While the applied finite-difference scheme authorizes a good automatic accounting for the details of the sediment-basement interface, different strategies were used by the three other groups: some used a rather coarse meshing that did not follow details of the valley boundaries, especially at shallow depth, while some others spent much time in refining the mesh. The 2 Hz maximum frequency considered here is still too low to actually clearly identify the effects of the valley boundaries, considering also the rather smooth velocity variation in the sediments and the absence of shallow weathered layers in the bedrock. This issue is presently investigated within the framework of another numerical comparative exercise on the Volvi–Euroseistest site in Greece, where both sediments and bedrock exhibit complex shallow structures with inner interfaces between different units.
- The effects of free-surface topography were found significant in elevated areas in the three surrounding mountain ranges, but less important within the valley. However, while they are negligible in the S1 case, they slightly increase in the W1 case corresponding to higher predominant frequencies. This result cannot therefore be extrapolated to frequencies higher than 2 Hz, and the question is still open.

The comparison of the numerical predictions obtained with the FDM, two implementations of the SEM, and ADER-DGM indicates that each of these methods can be applied to simulation of the earthquake motion in structurally complex sediment-filled valleys with the flat free surface. In addition to being methodologically relatively simpler than the SEM and ADER-DGM, the presented implementation of the FDM can be computationally more efficient because the volume harmonic averaging of moduli and volume arithmetic averaging of density allows to account for irregular interfaces in regular grids well-suited to parallel implementation, while abrupt changes in the grid size are also allowed at the transition between sediments and much stiffer bedrock. In the case of the presented predictions, the FDM needed approximately 65% of the computational time used by SEM, but obviously the difference may depend on the used computer and on the particular case under study. On the other hand, for the SEM and ADER-DGM the incorporation of the nonplanar free surface poses no methodological problem; thus, the methods can be equally easily applied to both the flat and nonplanar free surface. In general, it is far from easy and natural to implement free-surface condition in the FDM. The applied DSG Velocity-Stress FDM cannot account for the free-surface topography. If the incorporation of the topography is inevitable, for example, at particular sites and at higher frequencies, a hybrid combination with the finite-element method (Galis *et al.*, 2008) might be an alternative to the applied DSG VS FDM.

We would like to stress two main conclusions based on the ESG 2006 simulation exercise and the detailed comparison of the four closest numerical predictions:

1. No single numerical modeling method can be considered as the best for all important medium wave-field configurations in both computational efficiency and accuracy.

2. Reliable predictions of the earthquake ground motion in complex structures should be made using at least two different but comparably accurate methods to enhance reliability of the prediction. Our study indicates that the proper formulations and implementations of the FDM, SEM, and ADER-DGM can be applied.

Data and Resources

All data used in this article came from published sources listed in the references. The Fortran 95 computer code for performing the finite-difference scheme is available at www.nuquake.eu/Computer_Codes/ (last accessed June, 2010). A detailed description of the SEM1 software package can be found at www.geodynamics.org/cig/software/packages/seismo/specfem3d (last accessed June, 2010). A detailed description of the software package adopted for the SEM2 simulation can be found at http://geoelse.stru.polimi.it (last accessed June, 2010). The software CUBIT is available at http://cubit.sandia.gov/ (last accessed June, 2010).

Acknowledgments

This work was supported in part by the Slovak Research and Development Agency under the contract number APVV-0435-07 (project OPTIMODE) and VEGA Project 1/4032/07. All the computations using the SEM1 code were performed at the Service Commun de Calcul Intensif (SCCI) of the Grenoble Observatory. The authors providing the ADER-DG solutions thank the Deutsche Forschungsgemeinschaft (DFG), who supported the work through the Emmy Noether program (KA 2281/2-1). The cooperation of P. Bunge and J. Oeser for allowing the extensive use of the Tethys cluster is also gratefully acknowledged, as well as the support by the Leibniz Rechenzentrum in München. This comparison work was made possible through various financial helps and grants from ILL (Institut Laue-Langevin) and CEA (French Atomic Energy Commission) through the Cashima project, from the INTERREG IIIB Alpine Space Program of the European Commission through the Sismovalp project, and from the French National Research Agency (ANR) through the QSHA project.

References

Aki, K., and P. Richard (2002). *Quantitative Seismology*, Second Ed., University Science Books, Sausalito, California, 700 pp.

Anderson, J. G. (2004). Quantitative measure of the goodness-of-fit of synthetic seismograms, *13th World Conf. on Earthquake Engineering Conference Proc.*, Paper 243.

Canuto, C., M. Y. Hussaini, A. Quarteroni, and T. A. Zang (1988). *Spectral Methods in Fluid Dynamics*, Springer-Verlag, New York.

Chaljub, E. (2009). Spectral element modeling of 3D wave propagation in the Alpine valley of Grenoble, France, in *ESG 2006, Third Intl. Symposium on the Effects of Surface Geology on Seismic Motion*, P.-Y. Bard, E. Chaljub, C. Cornou, F. Cotton, and P. Guéguen (Editors), LCPC Editions, ISSN 1628-4704, Vol. 2**,** 1467–1473.

Chaljub, E., C. Cornou, and P.-Y. Bard (2009). Numerical benchmark of 3D ground motion simulation in the valley of Grenoble, French Alps, in *ESG 2006, Third Intl. Symposium on the Effects of Surface Geology on Seismic Motion*, P.-Y. Bard, E. Chaljub, C. Cornou, F. Cotton, and P. Guéguen (Editors), LCPC Editions, ISSN 1628-4704, Vol. **2,** 1365–1375.

Chaljub, E., D. Komatitsch, J.-P. Vilotte, Y. Capdeville, B. Valette, and G. Festa (2007). Spectral element analysis in seismology, in *Advances in Wave Propagation in Heterogeneous Media*, R.-S. Wu and V. Maupin (Editors), Vol. **365–419,** Elsevier Academic Press, New York.

Chapron, E., M. Dietrich, C. Beck, P. Van Rensbergen, P. Finckh, G. Menard, G. Nicoud, F. Lemeille, F. Anselmetti, and M. De Batist (2009). High-amplitude reflections in proglacial lacustrine basin fills of the NW Alps: Origin and implications, in *ESG 2006, Third Intl. Symposium on the Effects of Surface Geology on Seismic Motion*, P.-Y. Bard, E. Chaljub, C. Cornou, F. Cotton, and P. Guéguen (Editors), LCPC Editions, ISSN 1628-4704, Vol. 2**,** 1587–1596.

Cornou, C. (2002). Traitement d'antenne et imagerie sismique dans l'agglomération grenobloise (Alpes Françaises): Implications pour les effets de site, *Ph.D. Thesis*, (260 pages, www-lgit.obs.ujf-grenoble.fr/~cornouc/PUBLIS_CECILE/These_Version_Finale_Cecile.pdf), Joseph Fourier University, Grenoble (in French).

Cornou, C., P.-Y. Bard, and M. Dietrich (2003a). Contribution of dense array analysis to the identification and quantification of basin-edge-induced waves, part I: Methodology, *Bull. Seismol. Soc. Am.* **93,** 2604–2623.

Cornou, C., P.-Y. Bard, and M. Dietrich (2003b). Contribution of dense array analysis to the identification and quantification of basin-edge-induced waves, part II: Application to Grenoble basin (French Alps), *Bull. Seismol. Soc. Am.* **93,** 2624–2648.

Cornou, C., E. Chaljub, J. Verbeke, J. Converset, C. Voisin, L. Stehly, L. Margerin, S. Tsuno, J.-R. Grasso, P. Guéguen, S. Roussel, P. Roux, S. Hatton, and M. Campillo (2009). Measurement and variability study of site effects in the 3D glacial valley of Grenoble, French Alps, in *ESG 2006, Third Intl. Symposium on the Effects of Surface Geology on Seismic Motion*, P.-Y. Bard, E. Chaljub, C. Cornou, F. Cotton, and P. Guéguen (Editors), LCPC Editions, ISSN 1628-4704, Vol. **2,** 1621–1627.

Davis, P. and P. Rabinowitz (Editors) (1984). *Methods of Numerical Integration*, Academic Press, New York.

Day, S. M., J. Bielak, D. Dreger, R. Graves, S. Larsen, K. Olsen, and A. Pitarka (2003). *Tests of 3D Elastodynamic Codes: Final Report* *for Lifelines Project 1A02*, Pacific Earthquake Engineering Research Center, Berkeley, California.

de Basabe, J. D., and M. K. Sen (2007). Grid dispersion and stability criteria of some common finite-element methods for acoustic and elastic wave equations, *Geophysics* **72,** T81–T95.

de la Puente, J., M. Dumbser, M. Käser, and H. Igel (2008). Discontinuous Galerkin methods for wave propagation in poroelastic media, *Geophysics* **73,** T77–T97.

de la Puente, J., M. Käser, M. Dumbser, and H. Igel (2007). An arbitrary high order discontinuous Galerkin method for elastic waves on unstructured meshes IV: Anisotropy, *Geophys. J. Int.* **169,** 1210–1228.

Deville, M. O., P. F. Fischer, and E. H. Mund (2002). *High-Order Methods for Incompressible Fluid Flow*, Cambridge University Press, New York.

Dietrich, M., C. Cornou, G. Ménard, F. Lemeille, F. Guyoton, and R. Guiguet (2009). Seismic profiling and borehole measurements in the Isère Valley near Grenoble, France: 1—Data acquisition and processing, in *ESG 2006, Third Intl. Symposium on the Effects of Surface Geology on Seismic Motion*, P.-Y. Bard, E. Chaljub, C. Cornou, F. Cotton, and P. Guéguen (Editors), LCPC Editions, ISSN 1628-4704, Vol. **2,** p. 1597–1608.

Dumbser, M., and M. Käser (2006). An arbitrary high order discontinuous Galerkin method for elastic waves on unstructured meshes II: The three-dimensional case, *Geophys. J. Int.* **167,** 319–336.

Dumbser, M., M. Käser, and E. Toro (2007). An arbitrary high order discontinuous Galerkin method for elastic waves on unstructured meshes V: Local time stepping and *p*-adaptivity, *Geophys. J. Int.* **171,** 695–717.

Faccioli, E., F. Maggio, R. Paolucci, and A. Quarteroni (1997). 2D and 3D elastic wave propagation by a pseudo-spectral domain decomposition method, *J. Seismol.* **1,** 237–251.

Galis, M., P. Moczo, and J. Kristek (2008). A 3-D hybrid finite-difference–finite-element viscoelastic modelling of seismic wave motion, *Geophys. J. Int.* **175,** 153–184.

Gallovic, F., R. Barsch, J. de la Puente Alvarez, and H. Igel (2007). Digital library for computational seismology, *Eos* **88,** 559.

Gamond, J.-F., J.-P. Gratier, and F. Thouvenot (2009). Seismotectonic frame of the Grenoble Valley, in *ESG 2006, Third Intl. Symposium on the Effects of Surface Geology on Seismic Motion*, P.-Y. Bard, E. Chaljub, C. Cornou, F. Cotton, and P. Guéguen (Editors), LCPC Editions, ISSN 1628-4704, Vol. 2**,** p. 1569–1575.

Guéguen, P., C. Cornou, S. Garambois, and J. Banton (2007). On the limitation of the H/V spectral ratio using seismic noise as an exploration tool: Application to the Grenoble Valley (France), a small apex ratio basin, *Pure Appl. Geophys.* **164,** 115–134.

Guéguen, P., S. Garambois, S. Tadenuma, B. Lebrun, and F. Cotton (2009). Geotechnical, geophysical and seismological data used for the estimate of the highest amplified frequency in the basin of Grenoble, in *ESG 2006, Third Intl. Symposium on the Effects of Surface Geology on Seismic Motion*, P.-Y. Bard, E. Chaljub, C. Cornou, F. Cotton, and P. Guéguen (Editors), LCPC Editions, ISSN 1628-4704, Vol. 2**,** 1629–1637.

Harris, R. A., M. Barall, R. Archuleta, E. Dunham, B. Aagaard, J. P. Ampuero, H. Bhat, V. Cruz-Atienza, L. Dalguer, P. Dawson, S. Day, B. Duan, G. Ely, Y. Kaneko, Y. Kase, N. Lapusta, Y. Liu, S. Ma, D. Oglesby, K. Olsen, A. Pitarka, S. Song, and E. Templeton (2009). The SCEC/USGS dynamic earthquake rupture code verification exercise, *Seism. Res. Lett.* **80,** 119–126.

Jerram, J., P. Foray, S. Labanieh, and E. Flavigny (2009). Characterizing the nonlinearities of the lacustrine clays in the Grenoble basin, in *ESG 2006, Third Intl. Symposium on the Effects of Surface Geology on Seismic Motion*, P.-Y. Bard, E. Chaljub, C. Cornou, F. Cotton, and P. Guéguen (Editors), LCPC Editions, ISSN 1628-4704, Vol. 2**,** 1639–1648.

Käser, M., and M. Dumbser (2006). An arbitrary high order discontinuous Galerkin method for elastic waves on unstructured meshes I: The two-dimensional isotropic case with external source terms, *Geophys. J. Int.* **166,** 855–877.

Käser, M., M. Dumbser, and J. de la Puente Alvarez (2006). An efficient ADER-DG method for 3-dimensional seismic wave propagation in media with complex geometry, in *ESG 2006, Third Intl. Symposium on the Effects of Surface Geology on Seismic Motion*, P.-Y. Bard, E. Chaljub, C. Cornou, F. Cotton, and P. Guéguen (Editors), LCPC EditionsVol. 1**,** pp. 455–464, Grenoble.

Käser, M., M. Dumbser, J. de la Puente, and H. Igel (2007). An arbitrary high order discontinuous Galerkin method for elastic waves on unstructured meshes III: Viscoelastic attenuation, *Geophys. J. Int.* **168,** 224–242.

Komatitsch, D., and J. Tromp (1999). Introduction to the spectral element method for three-dimensional seismic wave propagation, *Geophys. J. Int.* **139,** 806–822.

Komatitsch, D., and J. P. Vilotte (1998). The spectral-element method: an efficient tool to simulate the seismic response of 2D and 3D geological structures, *Bull. Seismol. Soc. Am.* **88,** 368–392.

Komatitsch, D., Q. Y. Liu, J. Tromp, P. Suss, C. Stidham, and J. H. Shaw (2004). Simulations of ground motion in the Los Angeles basin based upon the spectral-element method, *Bull. Seismol. Soc. Am.* **94,** 187–206.

Komatitsch, D., R. Martin, J. Tromp, M. A. Taylor, and B. A. Wingate (2001). Wave propagation in 2-D elastic media using a spectral element method with triangles and quadrangles, *J. Comp. Acoustics* **9,** 703–718.

Komatitsch, D., S. Tsuboi, and J. Tromp (2005). The spectral-element method in seismology, in *Seismic Earth: Array Analysis of Broadband Seismograms*, A. Levander, and G. Nolet (Editors), American Geophysical Union Monograph 157, 205–228.

Kosloff, R., and D. Kosloff (1986). Absorbing boundaries for wave propagation problems, *J. Comp. Physics* **63,** 363–373.

Kristek, J., and P. Moczo (2003). Seismic-wave propagation in viscoelastic media with material discontinuities: A 3D fourth-order staggered-grid finite-difference modeling, *Bull. Seismol. Soc. Am.* **93,** 2273–2280.

Kristek, J., P. Moczo, and R. J. Archuleta (2002). Efficient methods to simulate planar free surface in the 3D 4(th)-order staggered-grid finite-difference schemes, *Stud. Geophys. Geod.* **46,** 355–381.

Kristek, J., P. Moczo, and P. Pazak (2009). Numerical modeling of earthquake motion in Grenoble basin, France, using a 4th-order velocity-stress arbitrary discontinuous staggered-grid FD scheme, in *ESG 2006, Third Intl. Symposium on the Effects of Surface Geology on Seismic Motion*, P.-Y. Bard, E. Chaljub, C. Cornou, F. Cotton, and P. Guéguen (Editors), LCPC Editions, ISSN 1628-4704, Vol. 2**,** p. 1517–1526.

Kristekova, M., J. Kristek, P. Moczo, and S. M. Day (2006). Misfit criteria for quantitative comparison of seismograms, *Bull. Seismol. Soc. Am.* **96,** 1836–1850.

Lebrun, B., D. Hatzfeld, and P. Y. Bard (2001). Site effect study in urban area: Experimental results in Grenoble (France), *Pure Appl. Geophys.* **158,** 2543–2557.

Liu, H. P., D. L. Anderson, and H. Kanamori (1976). Velocity dispersion due to anelasticity: Implications of seismology and mantle composition, *Geophys. J. Roy. Astron. Soc.* **47,** 41–58.

Lysmer, J., and R. L. Kuhlemeyer (1969). Finite dynamic model for infinite media, *J. Eng. Mech. Div. Proc. Amer. Soc. Civil Eng.* **95,** 859–877.

Maggio, F., and A. Quarteroni (1994). Acoustic wave simulation by spectral methods, *East–West J. Num. Math* **2,** 129–150.

Ménard, G., O. Blein, C. Fournier, A. Guyomard, C. Julian, J.-F. Gamond, and A. Paillet (2009). Relations between present vertical movements and sedimentary fill in the Grenoble area, in *ESG 2006, Third Intl. Symposium on the Effects of Surface Geology on Seismic Motion*, P.-Y. Bard, E. Chaljub, C. Cornou, F. Cotton, and P. Guéguen (Editors), LCPC Editions, ISSN 1628-4704, Vol. 2**,** 1577–1585.

Ménard, G., M. Dietrich, M. Vallon, S. Tadenuma, C. Bordes, O. Méric, F. Lemeille, and A. Paillet (2009). Seismic profiling and borehole measurements in the Isère Valley near Grenoble, France: 2—Interpretation, in *ESG 2006, Third Intl. Symposium on the Effects of Surface Geology on Seismic Motion*, P.-Y. Bard, E. Chaljub, C. Cornou, F. Cotton, and P. Guéguen (Editors), LCPC Editions, ISSN 1628-4704, Vol. 2**,** 1609–1620.

Mercerat, E. D., J. P. Vilotte, and F. J. Sanchez-Sesma (2005). Triangular spectral-element simulation of 2D elastic wave propagation using unstructured triangular grids, *Geophys. J. Int.* **166,** 679–698.

Moczo, P., and J. Kristek (2005). On the rheological models used for time-domain methods of seismic wave propagation, *Geophys. Res. Lett.* **32,** L01306.

Moczo, P., J.-P. Ampuero, J. Kristek, S. M. Day, M. Kristekova, P. Pazak, M. Galis, and H. Igel (2006). Comparison of numerical methods for seismic wave propagation and source dynamics—the SPICE Code Validation, in *ESG 2006, Third Intl. Symposium on the Effects of Surface Geology on Seismic Motion*, P.-Y. Bard, E. Chaljub, C. Cornou, F. Cotton, and P. Guéguen (Editors), LCPC Editions, Vol. 1**,** 495–504, Grenoble.

Moczo, P., J. Kristek, and M. Galis (2004). Simulation of the planar free surface with near-surface lateral discontinuities in the finite-difference modeling of seismic motion, *Bull. Seismol. Soc. Am.* **94,** 760–768.

Moczo, P., J. Kristek, M. Galis, P. Pazak, and M. Balazovjech (2007). The finite-difference and finite-element modeling of seismic wave propagation and earthquake motion, *Acta Phys. Slovaca* **57,** 177–406.

Moczo, P., J. Kristek, V. Vavrycuk, R. J. Archuleta, and L. Halada (2002). 3D heterogeneous staggered-grid finite-difference modeling of seismic motion with volume harmonic and arithmetic averaging of elastic moduli and densities, *Bull. Seismol. Soc. Am.* **92,** 3042–3066.

Moczo, P., J. O. A. Robertsson, and L. Eisner (2007). The finite-difference time-domain method for modeling of seismic wave propagation, in *Advances in Wave Propagation in Heterogeneous Media*, R.-S. Wu and V. Maupin (Editors), Vol. **421–516**, Elsevier Academic Press, New York.

Nicoud, G., G. Royer, J. C. Corbin, F. Lemeille, and A. Paillet (2002). Creusement et remplissage de la vallée de l'Isère au Quaternaire récent. Apports nouveaux du forage GMB1 (1999) dans la région de Grenoble (France), *Géologie de la France* **4,** 39–49 (in French).

Oeser, J., H. P. Bunge, and M. Mohr (2006). Cluster design in the Earth Sciences tethys, in *High Performance Computing and Communications—Second Intl. Conf., HPCC 2006*, Munich, Germany, Lecture Notes in Computer Science, vol. 4208**,** M. Gerndt and D. Kranzlmuller Vol. 31–40**,** Springer-Verlag Berlin.

Seriani, G., and S. P. Oliveira (2007). Dispersion analysis of spectral element methods for elastic wave propagation, *Wave Motion* **45,** 729–744.

Seriani, G., and E. Priolo (1991). High-order spectral element method for acoustic wave modeling, *Expanded Abstracts of the Soc. Expl. Geophys.* 1561–1564.

Seriani, G., and E. Priolo (1994). A spectral element method for acoustic wave simulation in heterogeneous media, *Finite Elem. Anal. Des.* **16,** 337–348.

Stacey, R. (1988). Improved transparent boundary formulations for the elastic wave equation, *Bull. Seismol. Soc. Am.* **78,** 2089–2097.

Stupazzini, M. (2009). 3D Ground Motion Simulation of the Grenoble Valley by GeoELSE, in *ESG 2006, Third Intl. Symposium on the Effects of Surface Geology on Seismic Motion*, P.-Y. Bard, E. Chaljub, C. Cornou, F. Cotton, and P. Guéguen (Editors), LCPC Editions, ISSN 1628-4704, Vol. **2,** 1551–1560.

Stupazzini, M., R. Paolucci, and H. Igel (2009). Near-fault earthquake ground motion simulation in the Grenoble Valley by a high-performance spectral element code, *Bull. Seismol. Soc. Am.* **99,** 286–301.

Thouvenot, F., J. Frechet, L. Jenatton, and J. F. Gamond (2003). The Belledonne Border Fault: Identification of an active seismic strike-slip fault in the western Alps, *Geophys. J Int.* **155,** 174–192.

Thouvenot, F., L. Jenatton, and R. Guiguet (2009). Seismicity of the Grenoble area, in *ESG 2006, Third Intl. Symposium on the Effects of Surface Geology on Seismic Motion*, P.-Y. Bard, E. Chaljub, C. Cornou, F. Cotton, and P. Guéguen (Editors), LCPC Editions, ISSN 1628-4704, Vol. 2**,** 1563–1567.

Titarev, V. A., and E. F. Toro (2002). ADER: Arbitrary high order Godunov approach, *J. Sci. Comput.* **17,** 609–618.

Tsuno, S., E. Chaljub, and P. Y. Bard (2009). Grenoble Valley simulation benchmark—comparison of results and main learnings, in *ESG 2006, Third Intl. Symposium on the Effects of Surface Geology on Seismic Motion*, P.-Y. Bard, E. Chaljub, C. Cornou, F. Cotton, and P. Guéguen (Editors), LCPC Editions, ISSN 1628-4704, Vol. 2**,** 1377–1433.

Vallon, M. (1999). Estimation de l'épaisseur d'alluvions et sédiments quaternaires dans la région grenobloise par inversion des anomalies gravimétriques, Unpublished IPSN/CNRS report, 33 pp. (in French).

Laboratoire de Géophysique Interne et Tectonophysique
CNRS
Observatoire de Grenoble, Université J. Fourier, France
Maison des Géosciences
BP 53, 38041 Grenoble
Cedex 9, France
Emmanuel.Chaljub@obs.ujf-grenoble.fr
Seiji.Tsuno@obs.ujf-grenoble.fr
bard@obs.ujf-grenoble.fr
(E.C., S.T., P.-Y.B.)

Faculty of Mathematics
Physics and Informatics
Comenius University Bratislava
Mlynska dolina F1
842 48 Bratislava, Slovakia
Peter.Moczo@fmph.uniba.sk
Jozef.Kristek@fmph.uniba.sk
(P.M., J.K.)

Department für Geo-und Umweltwissenschaften
Ludwig-Maximilians-Universität München
Theresienstrasse 41 80333 München, Germany
martin.kaeser@geophysik.uni-muenchen.de
(M.K.)

Department of Structural Engineering
Politecnico di Milano
Piazza Leonardo da Vinci, 32
20133 Milano, Italy
stupa@stru.polimi.it
(M.S.)

Geophysical Institute
Slovak Academy of Sciences
Dubravska cesta 9
845 28 Bratislava, Slovakia
kristekova@savba.sk
(M.K.)

Manuscript received 23 February 2009